UNIVERSITY OF COPENHAGEN
FACULTY OF SCIENCE

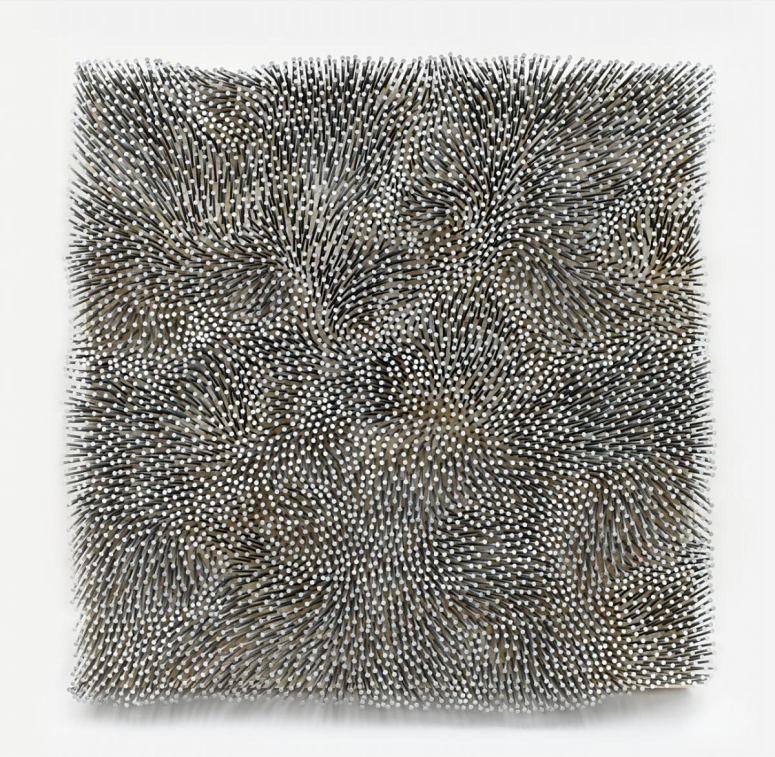

Master's thesis

Activity induced Patterns in Active Matter

Flow patterns in active fluids

Salik A. Sultan

Advisor: Amin Doostmohammadi

Submitted: February 15, 2022

Acknowledgment

Most importantly of all, I would like to thank my supervisor, Amin Doostmohammadi for the encouragement, support, and guidance throughout the thesis. Your passion for your research is contagious, and I am grateful to have felt both welcome and included in your research group. This thesis would not have been possible without Mehrana Raesian Nejad and Yavor Novev. You have both patiently provided me with many great ideas and helped me gain both perspective and insight. I would also like to thank my dear friends Mark Falkenstrøm, Nam Hai Tran, and Thea Quistgaard for helping proofreading the thesis. Finally, I would like to express my gratitude to my dear parents, sister, and brother for their invaluable emotional support during this whole process.

Abstract

The spontaneous emergence of collective flows is a generic property of active fluids and often leads to chaotic flow patterns characterised by swirls, jets, and topological disclinations in their orientation field. The main part of this thesis will explore a newly introduced active stabilising term to tame otherwise chaotic, active flows, showing how a balance between activity-induced order and disorder can act as a robust way of controlling and guiding active particles into dynamically ordered coherent structures. Here we find that the introduced term does stabilize active systems. Furthermore, we uncover a range of new exotic phases where topological defects self-organise into chains and aster-like structures. Additionally, we extend this framework to a discrete phase-field model of a cell monolayer by characterising the impact of chiral active stresses acting in between the cells. Here we explore the emergence of chiral edge currents and coherent patterns of motion of the cells in different configurations of confined geometry.

Contents

Chapter 1

Active nematics - The flow of nature

The work presented in this thesis intends to understand the dynamical behavior of soft matter systems categorised as active nematics. Active nematics conjoin the field of nematic liquid crystals with active matter and have two defining attributes: Firstly, the distribution and orientation of the constituting elements of an active system follow the physical laws of liquid crystals, a division of soft active matter, which at low temperatures form a nematic phase. Secondly, the individual elements constituting an active nematic system, locally convert energy into mechanical work, meaning that these systems belong in the division of active matter. Both of these concepts will be introduced and discussed in further detail in this opening chapter.

1.1 Overview

This chapter introduces the key underlying active nematics theory which makes up the foundation for the work done in this project. The rest of the thesis is constructed of two related studies on the topic of activity-induced collective behaviour in active fluids. Firstly, we will explore a newly introduced active stabilising term from equation 1.20. This is conducted by means of continuum simulations, and will explore new non-equilibrium states in active nematics by simultaneously varying the flow-aligning parameter χ, as well as the ratio between the dipolar activity ζ_1 and the new additional force quadrupolar term ζ_2. Secondly, the study is extended to a discrete phase-field model of a cell monolayer by characterising the impact of chiral active stresses acting in between the cells by introducing the chiral activity from equation 1.19. The coherent patterns of motion of the cells are explored in different configurations of confined geometry. Both the continuum and the phase-field models will be presented in Chapter 2. Chapter 3 will present the results from the continuum study and is the crux of the thesis. Chapter 4 will present the results of the phase-field study. Finally, Chapter 5 has a general summary and conclusion of the entire project.

1.2 Active matter

Active matter is a class of condensed systems out of thermodynamic equilibrium with the unifying characteristic that they are composed entirely of self-driven units or active particles. Each component of the system converts locally stored or ambient free energy into systematic movement. This is in contrast to most equilibrium systems, which rely on external contribution of energy [66, 82, 49, 57, 38]. Particles comprising an active matter system are often elongated and their direction of self-propulsion is set by their own anisotropy, rather than by an external field or geometric constraint. In nature, an orientational order can clearly be seen in different examples of macroscopic and microscopic active systems, such as swarms of bacteria, cell extracts of biofilament-motor protein [8], as well as cellular tissue [23, 40], schools of fish and flocks of birds [78], see Fig 1.1 for an illustration with active matter systems observed in nature at different length scales. Active matter is also found in non-living systems, on a variety of length scales, such as layers of vibrated granular rods, colloidal particles propelled through a fluid medium, and assemblies of robots [68]. Each element or particle of the active matter consumes and dissipates energy and this cycle fuels the internal changes which often result in motion. Such systems can be created in the lab with the aim of studying a simplified system capable of displaying collective motion whilst simultaneously being able to control parameters to gain insight into the governing properties of these systems [66].

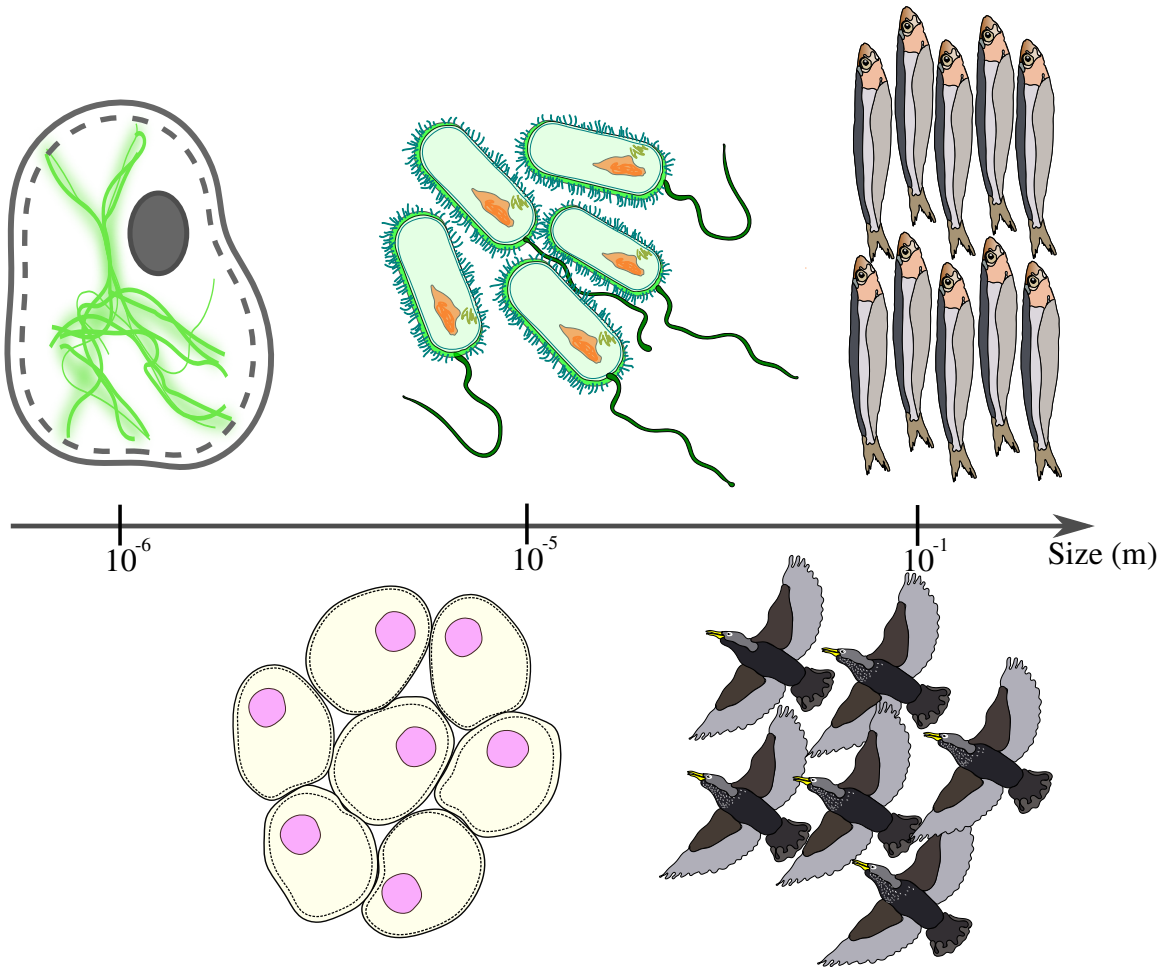

Figure 1.1: Scale showing illustrated examples of active systems at a variety of length scales. From left to right: Sub-cellular filaments, a cluster of cells, a grouping of swimming bacteria, a flock of birds, and a school of fish.

1.2.1 Pattern formation

Interactions, both internally between the active particles as well as the particles with a surrounding fluid, can give rise to distinct patterns. Patterns refer to the spontaneous formation of collective motion, or self-organization into highly ordered structures on much greater length scales than the individual unit in an otherwise quiescent system [2, 81, 81, 75, 30, 3].
Generally, well studied patterns can be categorised into three subcategories; polar patterns, nematic patterns, and clustering patterns. Polar patterns have a polar alignment of particles which means the particles are predominantly aligned and move unidirectionally. These patterns are often linked with transport and can also appear as swirls or jets. Polar jets of swimming bacteria have been shown to transport microscopic cargo [79]. Nematic patterns are defined as structures in which particles move bidirectionally, sometimes anti-parallel, along the alignment director. Nematic ordered filaments have been studied in microtuble-based active gels in [66]. Active systems can also form clustering patterns, such as phase-separation or motility-induced formation of colonies [62].

1.2.2 Wet and dry systems

In order to understand mechanisms behind diverse behaviours of active materials, it is often useful to divide active systems into two general categories: wet and dry active matter. In *wet active matter*, flows created by the particles mediate long-range hydrodynamic interactions in the system [42] such as in unconfined suspensions of filaments and motor proteins [57, 45], bacterial suspensions in low concentrations [79], and collection of artificial active colloids suspended within a fluid medium [9].

On the other hand, the collective behaviour of dry active materials is governed by direct interactions, such as collision between active particles [68, 14]. Shaken granular matter [39, 44] and bacteria moving on a substrate [53] are examples of *dry active matter*. Descriptions based on dry active matter theories have been helpful in investigating the different patterns in clusters of bacteria which live on dry surfaces in tight spaces [63, 32].

1.3 Liquid crystals

Liquid crystals are an intermediate phase between a liquid and a crystal, which are comprised by mesogens; the anisotropic rod-like elementary molecules or units that make up the crystal. The crystals exhibit both solid-like properties, such as elasticity, as well as liquid-like properties, such as fluidity. Liquid crystals are in thermodynamical equilibrium and have different mesogenic phases of matter, not limited to, but most notably: crystalline solid, isotropic liquid and nematic liquid crystal. It is important to note that different matter can exhibit both different transitions between phases of matter and other phases of matter. In the *isotropic phase*, illustrated in Fig 1.2.c, the mesogens can take any orientation or position in the formation. In the *nematic phase* the mesogens have an orientational order but no positional order. This means that mesogens align along the unit vector n

known as the director (Fig 1.2.b). Given the orientaional order, the mesogens do not have a positional constraint and can move freely within the liquid. At the lowest temperature, the liquid form the *crystalline phase*. Here the configuration has the mesogens in a fixed alignment side-by-side in assembled layers (Fig 1.2.c).

1.3.1 Director field and order

The molecules in the nematic phase tend to have some order by being parallel to a unit vector $\hat{n}$ (see dashed line in Fig 1.2.b). The unit vector $\hat{n}$ is a headless vector, meaning that $\hat{n}$ and $-\hat{n}$ are indistinguishable. This defines the average orientation of the liquid crystal volume and is known as the director field. The director field is in a nematic state, is apolar, and head-tail symmetric. It is noteworthy to clarify that the magnitude of the director describes the united direction of the system, rather than locally for the individual particle. To describe the orientational order, we study the evolution of a traceless rank-2 tensor $\mathbf{Q}$, known as the nematic order parameter. It takes the form

$$\mathbf{Q} = 2q(\hat{n}\hat{n}^{\intercal} - \frac{\mathbf{I}}{2}), \tag{1.1}$$

where q and $\hat{n}$ show the magnitude and orientation of the order, respectively, and $\mathbf{I}$ represents the identity tensor. The orientation on the order $\hat{n}$, can be described as

$$\hat{n} = [\cos\theta, \sin\theta], \tag{1.2}$$

where θ is the director angle. We can define the magnitude of the particle alignment using a probability density function $f(\theta, \phi)$, here ϕ is a polar angle. Assuming a cylindrical symmetry around $\hat{n}$, the distribution function $f(\theta, \phi)$ loses its dependency on ϕ. Furthermore, the head-tail symmetry of the particle means equivalence in directions $\hat{n}$ and $-\hat{n}$, and it follows that $f(\theta) = f(\theta - \pi)$. Due to this equivalence, there is no average dipole and we instead use the Legendre polynomial for multipole expansion. The next multipole, the quadrupole, is defined as

$$q = \frac{1}{2N}\langle(3\cos^2\theta - 1)\rangle = \int_{-\pi/2}^{\pi/2} f(\theta)\frac{1}{2}(3\cos^2\theta - 1)d\Omega, \tag{1.3}$$

with N representing the number of particles [18]. The expansion allows for evaluation of the magnitude of alignment.

1.3.2 Nematic ordering in liquid crystals

In thermodynamic equilibrium, isotropic and nematic states in liquid crystals are the minima of a free energy $\mathcal{F}$. Based on the symmetry of the Q-tensor, a Ginzburg-Landau free energy can be defined. This is known as a Landau-de Gennes free energy in nematic liquid crystals and this description is possible due to the symmetry of the Q-tensor, where the free energy is the volume integral of a local function based on Q as well as its derivatives [18]. The Landau-de Gennes expression is presented in terms of expansions of Q as well

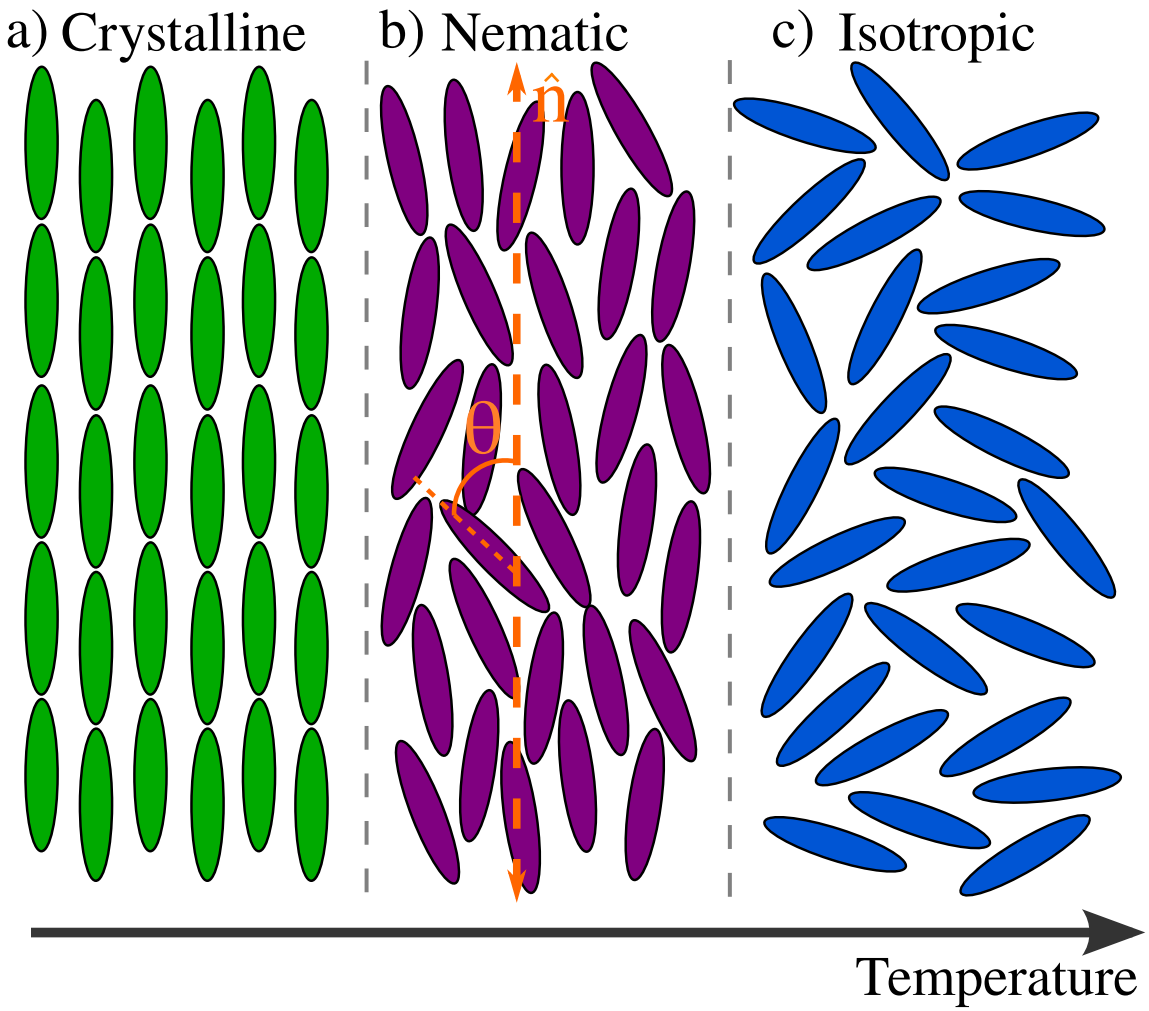

Figure 1.2: Illustration of a liquid crystal mesogen system displaying different phases of matter. a) Crystalline solid state has the mesogens in a fixed positional and orientational distribution. b) Nematic phase has no positional order, but an orientational order along its director n. The orange dashed line indicates the nematic alignment along the director n and orientational angle θ. c) An isotropic liquid crystal has no order in both position and orientation, the distribution of mesogens is random. Figure interpolated from P. Collings [Princeton University Press [15]]

as expansions in derivatives of Q which represent the bulk free energy density $\mathcal{F}_b$ and the gradient free energy density $\mathcal{F}_g$ respectively.

The sole rotational invariant function of a two dimensional tensor is $\mathrm{tr}(Q^2)$. Thus, we can express the bulk free energy density as

$$\mathcal{F}_b = \frac{\mathcal{A}}{2}\mathrm{tr}(Q^2) + \frac{\mathcal{B}}{4}(\mathrm{tr}(Q^2))^2, \tag{1.4}$$

where $\mathcal{A}$ and $\mathcal{B}$ are known as Landau-de Gennes co-coefficients. The gradient free energy density $\mathcal{F}_g$ is defined by

$$\mathcal{F}_g = \frac{L_1}{2}\partial_k Q_{ij}\partial_k Q_{ij} + \frac{L_2}{2}\partial_k Q_{kj}\partial_i Q_{ij}, \tag{1.5}$$

where L_1 and L_2 are the elastic constant penalizing deformations in the director field.

1.3.2.1 Elasticity in liquid crystals

A system of nematic molecules can acquire elasticity as a response to distortions from a perfectly aligned state. In two-dimensional nematics, most distortions can be attributed two different base distortions; splay (Fig 1.3.A), and bend (Fig 1.3.B). The increase in free energy density, which is a consequence of distortions from the aligned state, is referred as the Frank free energy. This elastic free energy can be defined in terms of the director $\hat{n}$:

$$f_{elasticity} = \frac{K}{2}\int d^2\underline{r}|\nabla\theta|^2 \tag{1.6}$$

where K is the elastic modulus of the nematic liquid crystal. Nematic liquid crystals prefer to stay uniformly aligned and distortions in the system are penalised through the elastic free energy.

1.3.3 Topological defects

In two dimensions, orientational fields can have disclinations; discontinuities in the director field. These are known as topological defects and represent a local singularity in the liquid crystal phase. Discontinuities can be point defects, which are located at a point, or on a line as disclination lines. As this thesis is focused on two-dimensional nematics, only point defects are considered. The minimization of equation 1.6 reveals distortions in the form

$$\theta(\underline{r}) = s\phi(\underline{r}) + \theta_0, \tag{1.7}$$

where $\phi(\underline{r})$ is the polar angle and θ_0 is the off-angle (canting angle) representing the possible configurations of a defect with charge s. The charge or strength of the defect is classified by a winding number s, which is defined as

$$s = \frac{1}{2\pi}\oint_S d\theta, \tag{1.8}$$

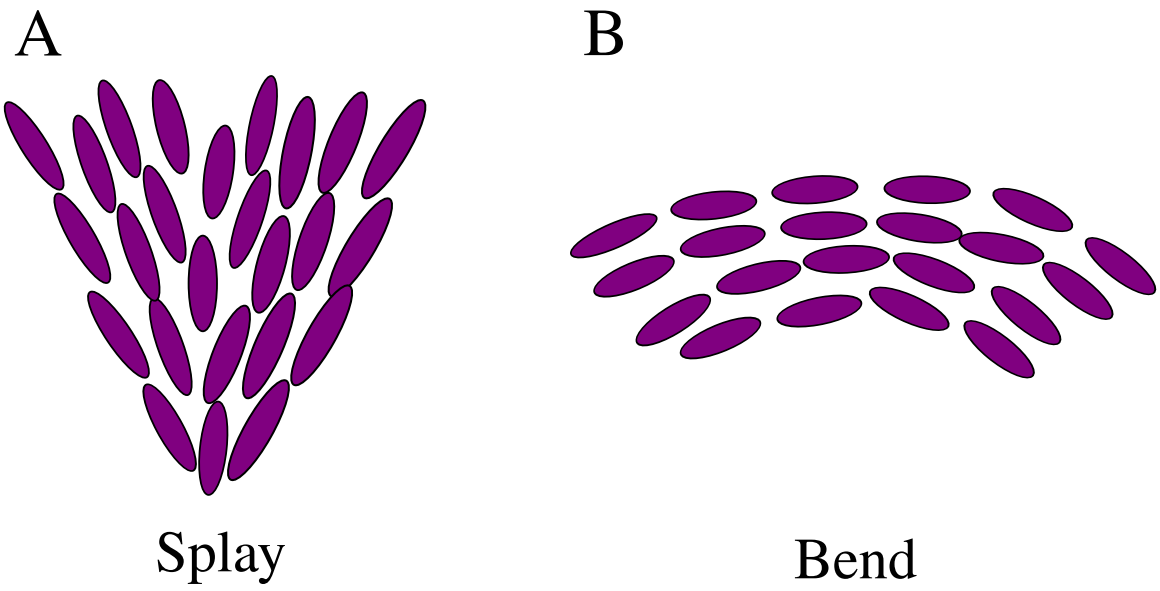

Figure 1.3: Particle configurations of the elementary deformation for (A) Splay and (B) Bend distortions.

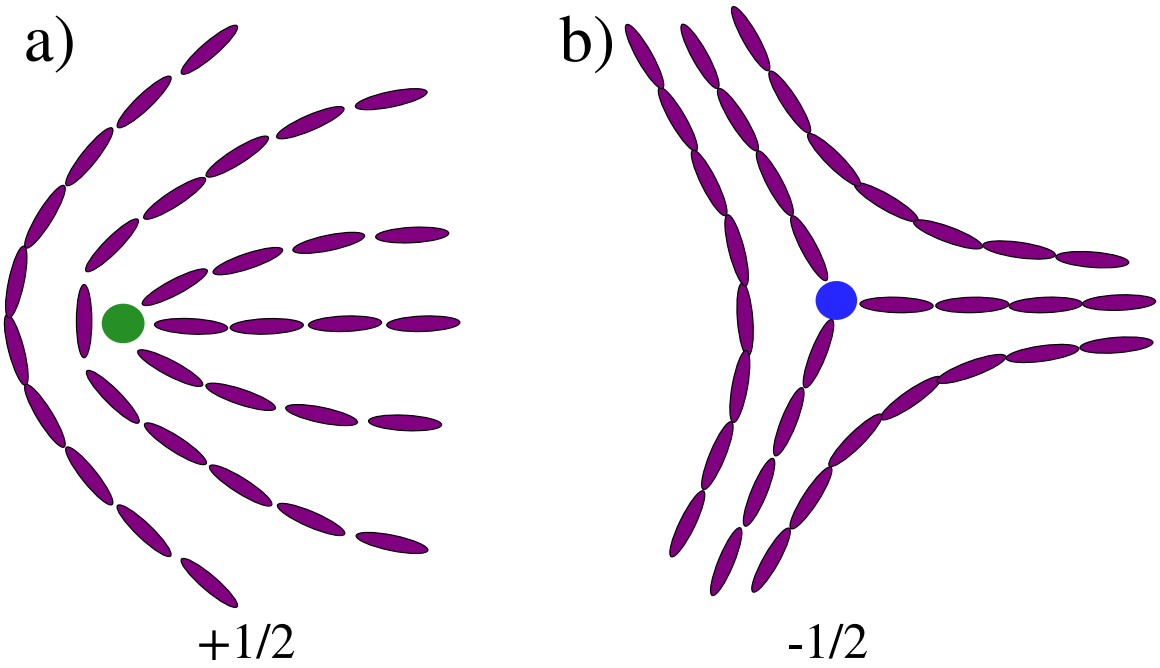

Figure 1.4: Illustration showing the mesogen configuration of the a) Comet-like (+1/2) and b) trefoil-like (-1/2) topological defect. The green (blue) dot symbolises the core of the +1/2 (−1/2) defect.

representing the angle of orientation the director must rotate when circumnavigating along a contour of the defect core. S is a loop in a two dimensional plane. The predominant, simplest, and lowest topological charge comes in the form of the comet-like $+1/2$ (Fig 1.4.a) and trefoil-like $-1/2$ defects (Fig 1.4.b) [18]. Here the $\pm 1/2$ refers to the orientation angle the nematic rotates when circumnavigating around the defect core and the green and blue dots represent the defect cores. Defects with a higher charge are outside the scope of this thesis and will therefore not be covered. Higher order (full-integer) defects are covered in following references [5, 43]

Topological defects in passive liquid crystals can be attributed to external energy input into the molecule in the form of distortions to the director. As liquid crystals are in thermodynamic equilibrium, any external energy stored in topological defects must be released, and thus, the defects would vanish. Experimental setups, which are generally conducted using constrained finite systems, have obvious boundary conditions, since experimental setup cannot be infinitely large. These boundary constraints to the director field can lead to perturbations to the alignment of the mesogens creating conditions for the formation of topological defects.

1.4 Nematohydrodynamics

The flow of liquid crystals is coupled to the orientation of nematic mesogens (nematogens). The relationship can be described as such; flow disturbs the nematic alignment just as well as the response from distortions in the orientational field leads to flow. A hydrodynamic theory, which couples the fluid velocity with the nematic director in terms of the tensor order parameter Q, was developed by Beris, Edwards, and Grmela [10, 26].

1.4.1 Beris-Edwards formulation

The nematohydrodynamic equations of motion are based on symmetry, have a close affinity to the Navier-Stokes equations, and can be used to describe the 2D dynamics of $\mathbf{Q}$ combined with the density of a suspension ρ as well as the velocity of the surrounding fluid $\mathbf{u}$.

$$(\partial_t + u_k \partial_k) Q_{ij} - S_{ij} = \Gamma H_{ij} \tag{1.9}$$

$$\rho(\partial_t + u_k \partial_k) u_i = \partial_j \Pi_{ij} - f u_i; \quad \partial_i u_i = 0. \tag{1.10}$$

f is the friction coefficient. The stress tensor Π_{ij}, is comprised of different stresses, and will be covered in more detail later in this chapter. Γ is the rotational diffusivity which, along with the molecular field H_{ij}, is the governing property describing the relaxation of the $\mathbf{Q}$ - tensor where

$$H_{ij} = -\frac{\delta \mathcal{F}}{\delta Q_{ij}}. \tag{1.11}$$

The orientation relaxation is governed by the total free energy $\mathcal{F}$, which is the sum of equations 1.4 and 1.5 and is defined by

$$\mathcal{F} = \frac{A}{2}(q^2 - \mathbf{Q} : \mathbf{Q})^2 + \frac{K}{2}|\nabla \mathbf{Q}|^2 + g(\nabla \cdot [\nabla \cdot \mathbf{Q}])^2. \tag{1.12}$$

Here, : denotes the double product of the two tensors. The free energy includes a nematic alignment term (with coefficient A) and an elastic term which penalises gradients in the $\mathbf{Q}$ tensor. Here, a singular elastic constant approximation is used and is shown by the elastic constant by K. In line with previous studies of dry active nematic [59, 65], we also include a regularization term with coefficient g which provides stability to our numerical solutions at small length scales. S_{ij} is the generalised non-linear advection term which describes the relationship between a nematic order and its corresponding velocity gradient and is defined as

$$S_{ij} = \chi E_{ij} + \left[Q_{ik} + \frac{\delta_{ik}}{2}\right]\Omega_{kj} - \Omega_{ik}\left[Q_{kj} + \frac{\delta_{kj}}{2}\right] \tag{1.13}$$

Here $E_{ij} = (\partial_i u_j + \partial_j u_i)/2$ is the strain rate tensor and $\Omega_{ij} = (\partial_j u_i - \partial_i u_j)/2$ is the vorticity tensor. The aligning parameter χ drives the relationship between the magnitude and orientation of the nematic order $\mathbf{Q}$ and the velocity gradient. This determines whether the system is in a flow tumbling or flow-aligned regime [73]. In a flow tumbling regime, the director tumbles under shear flow while in a flow aligning regime it aligns with an angle (Leslie angle) with the direction of the shear [10].

1.5 Active nematics

In order to mimic and understand the mechanisms behind natural active materials, several approaches have been suggested. The approaches to study the collective behaviour of active matter have come in the form of both experimental and theoretical model systems [18]. One particular thoroughly studied class of active matter can be simplified to groupings comprised of elongated rod-shaped particles. Examples of this class include elongated bacteria and inter-cellular filamentous particles. These particles are active and share a resemblance to the aforementioned nematic liquid crystals, which are comprised by elongated molecules and characterised by long-range orientational order. This resemblance has given rise to the concept of *active nematics* that adapts and applies central theories from our understanding of the physics of liquid crystals to the field of active matter.

1.5.1 Active stress

At the microscopic level, the force exerted by a single active particle on its surrounding fluid can be represented as a force dipole. Collectively, a large number of force dipoles give rise to a symmetric active stress, which turns the system out-of-equilibrium. Topological defects in an active nematic system are formed due to the active stresses acting on the individual system components, which distort the director field. These instabilities are exaggerated or mended depending on the type of elements that make up the active nematic system.

1.5.2 Dipolar extensile and contractile systems

The force distribution acting on an active particle is in its simplest form considered a force dipole. Using the same bacteria example from [50], the rotation exerted by the flagella as well as the counter rotation from the body would push the surrounding fluid away along its axis of direction (Fig 1.5.A). These particles are known as pusher or extensile particles and are represented as a force dipole with the red arrows indicating the direction of force. Extensile systems comprise elements that pump the surrounding fluid in an outwards direction along their symmetry axis n and inwards in the direction perpendicular to n. Contrarily, a puller in a contractile system, causes elements to pump fluid inwards along n and outwards in a direction perpendicular to that. This would be similar to Fig 1.5.A with the signs reversed.

As a result of the flows created in active suspension in the bulk, an extensile system is stable under splay deformation and unstable under bend deformation [3]. Contrarily, a contractile system is stable under bend deformations, but unstable as a result of splay deformations [72] [74]. This flow can be incorporated into the stress component Π_{ij} of nematohydrodynamics equations 1.9 and 1.10. The momentum density in a momentum conserving system is defined as

$$\partial_t(\rho u_i) = -\partial_j \Pi_{ij}, \tag{1.14}$$

where Π is the stress tensor. The particles are self-propelling without any outside forces acting upon them. Thus, according to Newton's third law, the force exerted by the particle on the fluid, must be equal to the force exerted on the particle by the fluid. Generally, the stress tensor in equation (1.9) for the nematic fluid is comprised of different stresses; this includes viscous, passive and active contributions

$$\Pi_{ij} = \Pi_{ij}^{\text{Viscous}} + \Pi_{ij}^{\text{Passive}} + \Pi_{ij}^{\text{Active}}. \tag{1.15}$$

$\Pi_{ij}^{\text{Viscous}}$ is the stress tensor representing the viscous contribution

$$\Pi_{ij}^{\text{Viscous}} = 2\eta E_{ij}, \tag{1.16}$$

where η determines the fluid viscosity of the surrounding fluid or suspension. The passive contribution $\Pi_{ij}^{\text{Passive}}$ is defined as

$$\Pi_{ij}^{\text{Passive}} = -P\delta_{ij} - \lambda S H_{ij} + Q_{ik}H_{kj} - H_{ik}Q_{kj}, \tag{1.17}$$

and represents the passive, elastic stresses. P denotes the bulk pressure. These stresses impact the director dynamics by altering the defect motility and trajectory [29]. The active stress contribution to the stress tensor leads the active particles to act as force dipoles and is defined by[2] as

$$\Pi_{ij}^{\text{Active}} = -\zeta Q_{ij}, \tag{1.18}$$

here ζ is the activity strength, which determines the intrinsic vorticity-relating length-scale set by the activity of the fluid. An active nematic system destabilizes as a consequence of the dipolar force exerted on the surrounding fluid. Systems where $\zeta > 0$ are known as extensile systems and systems where $\zeta < 0$ are known as contractile systems.

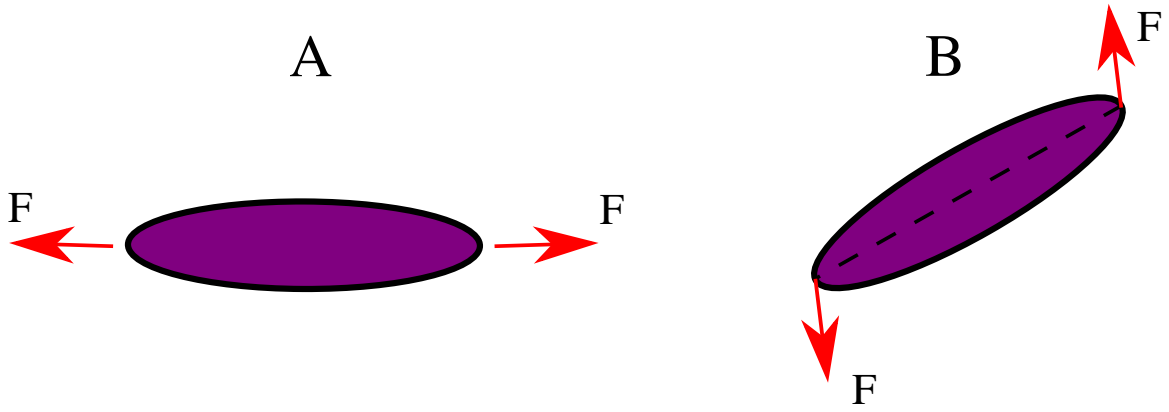

Figure 1.5: Illustration of an elongated particle. The red arrows indicate the force for A) force dipole of an extensile particle and B) Torque dipole of a chiral particle. Interpolated from [50].

1.5.3 Torque dipoles and chirality

Although the active stress created from a force dipole is considered achiral, there have been multiple systems studied where the surrounding fluid and particle rotate in opposite directions. This gives rise to the possibility of a *torque dipole* in addition to the force dipole. Torque dipoles are represented as two equal and opposite point torques, separated by some distance, see Fig 1.5. This can be considered the simplest microscopic description of a chiral active particle. Chirality in biological systems has been studied microscopically in force dipoles. For example rotating flagella on cells and other microorganisms have been attributed to microscopic torque dipoles. This gives rise to anti-symmetric stresses which govern chiral patterns such as rotating flows. These stresses have been shown analytically for cell monolayers [36], where the active stress tensor is described in terms of the tensor order parameter Q_{ij}

$$\sigma^{\text{chiral}} = -\zeta_\tau \epsilon_{ik} Q_{kj}, \tag{1.19}$$

where ζ_τ is the activity governing the chiral activity. The effects of this activity are studied in Chapter 4.

1.5.4 Role of active forces in stabilization

Active matter systems destabilize as a result of the active forces which exert a dipolar force distribution on the surrounding fluid by the active particles [48]. The schematic in Fig 1.6.A and B shows both signs of dipole force distributions destabilizing an ordered bend or splay configuration. When an active particle is in contact with a substrate or under extreme confinement, the dipolar stress is screened and a higher order quadrupolar contribution also becomes important [52]. In this vein, a recent study has introduced the coarse-grained continuum representation of quadrupolar forces as an additional non-equilibrium active

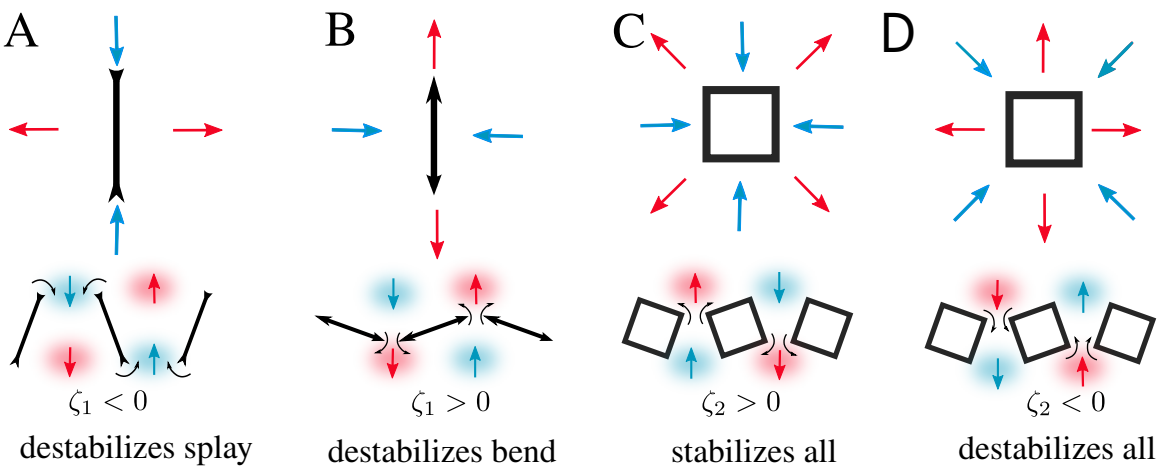

Figure 1.6: Schematic from [48] illustrating the active forces' effect on the stability of surrounding fluid. (A) Top: A contractile particle, also known as a "puller", which pumps the surrounding fluid inwards along its long axis (blue arrows) and outward along its short axis (red arrows). Bottom: In a system with a splay configuration, the contractility of the particle results in a flow (red and blue arrows) which drags the particles and accentuates the disrupted configuration further by rotating in accordance with the thin black curving arrows. (B) Top: A contractile particle, also known as a "pusher", has the opposite force dipole and further destabilizes bend configurations. (C) (D) Quadrupolar active force present in active systems at higher multipoles of the force density distribution. For a positive (negative) sign the resulting force flow of this configuration stabilizes (destabilizes) the active particle in both dipolar destabilization associated with bend and splay configurations.

force that is generated by dense suspension of active particles [48]. The argument presented in this paper suggests that force distributions of a higher angular symmetry do not cause the ordered phase to destabilize. They consider a square shape with a quadrupolar force distribution, pulling the fluid to its face and pushing it to the corners. A perturbation in a system comprised of such particles would lead to bunching in some areas. This would correct itself as the fluid would flow from the space created by the bunching of particles, pushing them back into alignment. Including the quadrupolar contribution, the stress tensor from equation 1.9 is now defined as

$$\Pi^{\text{Active}} = -\zeta_1 Q_{ij} - \zeta_2 Q_{ij} \cdot (\partial_k Q_{kj}). \tag{1.20}$$

ζ_2 is the activity parameters for the stabilising quadrupole activity. Note that the dipolar activity ζ from equation 1.18 has been renamed ζ_1 to easier distinguish the different active coefficients. In addition to the well-established dipolar activity, the force distribution of the higher angular symmetry, the force quadrupole term with coefficient ζ_2 in equation 1.20, becomes important in systems in contact with a substrate, where the momentum is not conserved [48].

1.5.5 Active turbulence

In contrast to passive, molecular or colloidal nematic liquid crystals, the particles comprising an active system have an activity. This activity, which causes inhomogeneties in the system, can result in conditions where inconsistencies in the domain cause a directional mismatch. Such inconsistencies can result in singularities in the order, i.e. topological defects, in a similar fashion to nematic liquid crystals. This causes the destruction of long ranged nematic order and can lead to the formation of chaotic systems such as active turbulence. When the number of active particles in a system increases, their interactions become stronger and can dominate over the dynamics of a singular unit. This can lead to the phenomenon *active turbulence*.

Active turbulence is a state characterised by its chaotic flow-fields, systematic fluctuations in the form of continuous jets, swirls and vorticies. Numerical simulations have shed light on the mechanisms behind the development of active turbulence in active materials [74, 76]. Systems in a nematic state with a slight perturbation begin to destabilise as the perturbations grow larger due to hydrodynamic instabilities. In the director field these deformations localise to form walls of bend deformations, separating the nematic regions and undulating a pair of oppositely charged $\pm 1/2$ defects as a result of the elasticity and active stress of the system. Flow separates the defect pair as the nematic field around the defects generates active stresses. The dynamics of both the walls and defects become chaotic and defects of opposite signs annihilate creating stability and restoring nematic order in the system. [20, 74]. See Fig 1.7 for a visual evolution of this process.

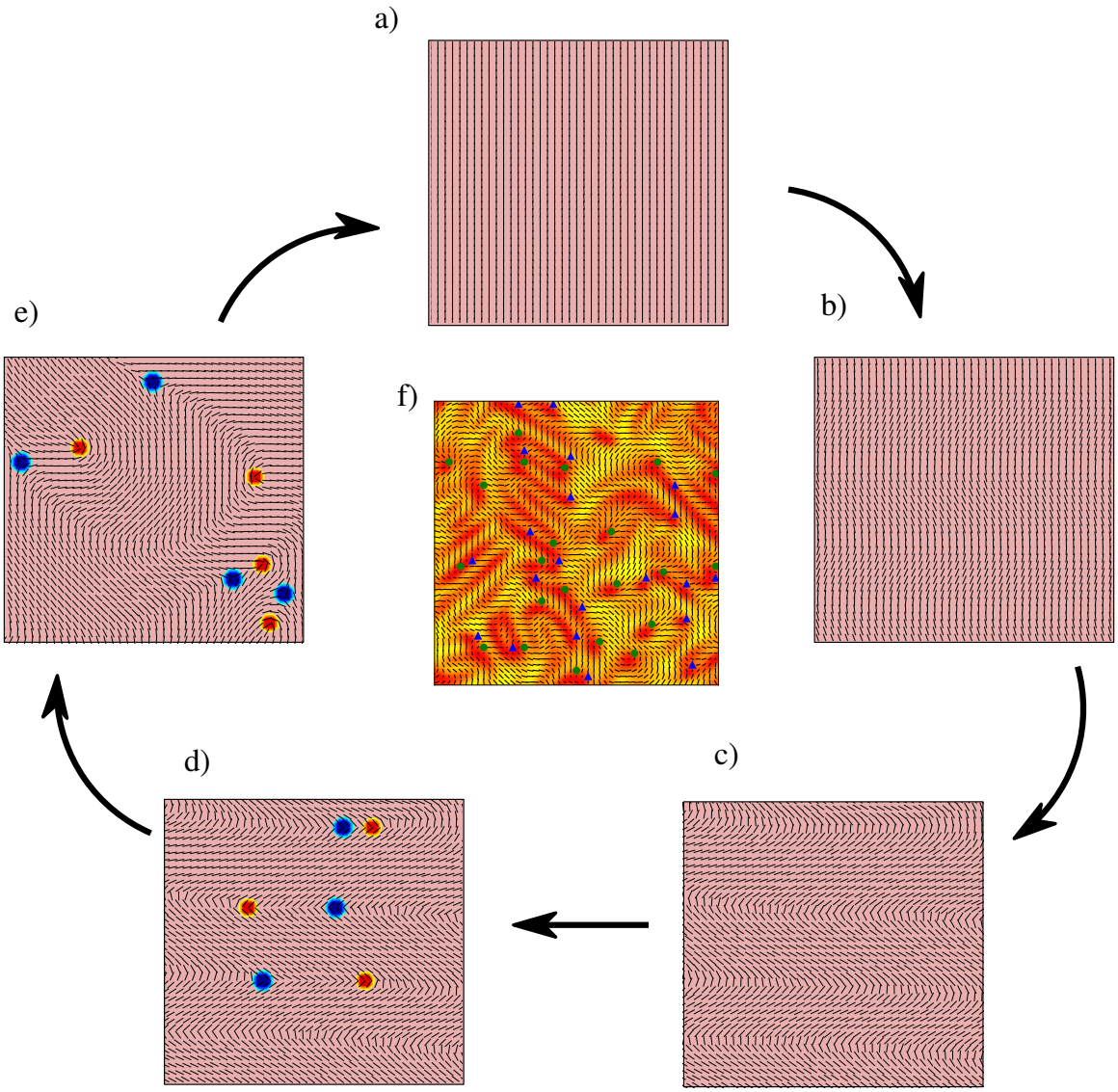

Figure 1.7: Evolution of turbulence taken and modified from [76]. a) Ordered system. b) and c) formation of walls, which fluctuate and decay into d) topological defects. The defects here are marked red and blue for $+1/2$ and $-1/2$ respectively. e) Defects annihilate and restore the nematic order. The pink underlying colour is just for ease visual interpretation of the director. f) Snapshot of a simulation of active turbulence. The system has many defects and is characterised by disorder in the domain. The $+1/2$ ($-1/2$) defects are marked by green (blue), and the underlying colour map represented the magnitude of order, with red being the lowest and yellow the highest.

1.5.5.1 Taming of active turbulence

Due to the widespread implications in biological processes and in design of non-equilibrium materials, there is a great interest in control and stabilization of active materials [72, 57, 74, 20]. On that account, several theoretical and experimental mechanisms have been proposed to tame the otherwise chaotic motion of active particles [33, 71, 22]. In particular, topological [41, 54] and geometrical [34] constraints have shown to be particularly successful in streamlining flows of active particles. Mechanistically, such constraints induce hydrodynamic screening effects that allow for stabilisation of active flows. For example, placing bacterial suspensions or microtubule-motor protein mixtures under confinement is shown to result in a crossover from chaotic flows to vortex-lattices and coherent streams as the confinement size decreases [34, 83]. Similarly, placing active particles in contact with substrates results in a friction-induced screening length that could stabilise chaotic flows into vortex-lattices [19, 77]. The taming of active turbulence is one of the primary motivations for the work presented in Chapter 3.

1.5.6 Collective behavior in active nematics

There are a number of well-studied examples of large-scale collective behaviour found in different cellular and bacterial systems within the field of active nematics. Poujade et al. have shown collective migration of a cellular monolayer of Madin-Darby Canine Kidney cells. The experiments, inspired by wound-healing, show long-range collective motion of cells would be triggered when exposed to a free surface [64]. A study by Meacock et al. 2020 found that the physics of active liquid crystals explain how slow-moving bacteria can expand faster when competing with faster-moving counterparts [53]. Furthermore, cohesive flow patterns have been observed in geometrically confined sub-cellular filaments. Wu et al. have shown how fluids display organised and unidirectional flow, independent of geometric scale, when confined into toroidal channels and cylindrical domains [84]. Collective motion of sperm has been shown to display turbulent behaviour in terms of long-range whirlpool-like structures [17]. Turbulent behaviour has also been found in human bronchial epithelial cells [11]. For further examples of experimental studies of collective motion in active nematics, see following review articles [20, 2, 31, 21].

1.5.7 Collective behaviour in cells

Having covered general examples of collective behaviour in active systems, we turn to a well-studied area of experimental active nematics; the collective behaviour in cells. Cell systems are highlighted as the work in Chapter 4, takes a cell-based modelling approach to investigate activity induced collective behaviour. The collective motion of cells is known to impact physiological and pathological conditions in epithelial cells, such as embryonic morphogenesis, wound healing and cancer invasion [35, 27, 13]. Fluctuations in systems consisting of cells have also been found to display properties of liquid crystals, specifically, in the form of local nematic alignment and topological defects [80]. Motivated by the

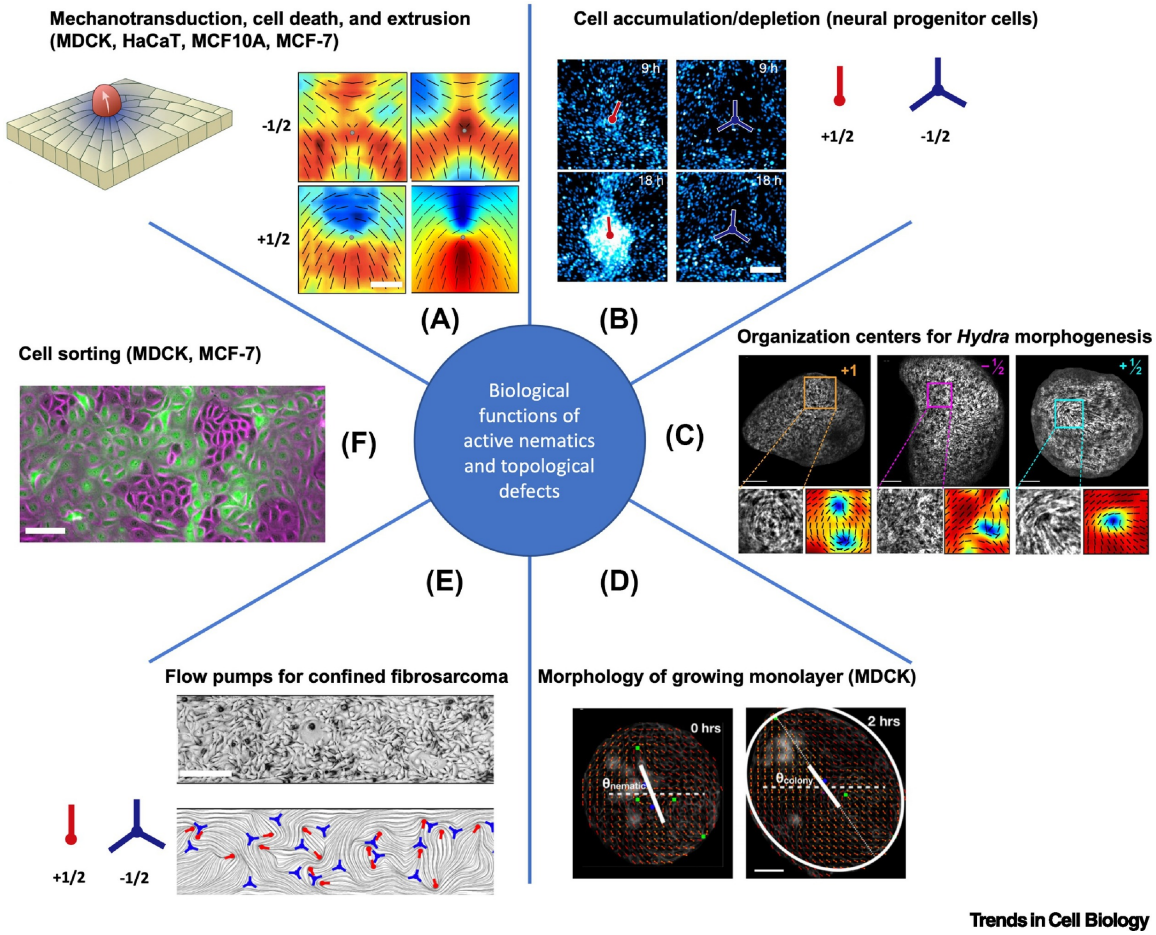

Figure 1.8: Collection of images from different experimental cell systems which all exhibit collective behavior that can be explained by active nematics. a) Death and extrusion provoked by topological defects in epithelial cell alignments [67]. b) Defects of charge $+1/2$ (red) and $-1/2$ (blue) in a monolayer of neural progenitor stem cells (Nature Publishing Group) [40]. c) Topological defects found in the nematic order of actin fibres [51]. d) Elongation of a growing epithelial tissue [16]. e) Topological defects of charge $+1/2$ (red) and $-1/2$ (blue) in confined fibrosarcoma cells [85]. f) Cell sorting driven by change in nematic behaviour of cellular monolayer[7]. Collage image taken from [21].

evidence of a coupling between the collective dynamics of epithelial cells and the theories of active liquid crystals, models of dense cellular monolayers have been developed in order to simulate the collective behaviour of cells with active inter-cellular forces [55, 86, 37]. Physical properties of cells, such as motility or shape, have shown a variety of different dynamical behaviours such as chaotic flows as well as jamming [28, 60], and edge migration [85]. See Fig 1.8 for examples of nematic behaviour in cell systems.

1.6 Concluding remarks

This chapter introduced the foundations of active nematics. Specifically, it introduced the active forces which are key in the studies done in this thesis, namely the quadrupolar active force from equation 1.20 and chiral active force from equation 1.19. As stated in section 1.5.4, the quadrupolar contribution can stabilize active particles associated with bend or splay configurations. Understanding the stability of active nematics, is of vital importance in the pursuit of harnessing the full potential of active materials. An example is a study where bacterial jets were stabilized in space such that they could carry microscopic cargo [79]. Theory and experiments are inseparably for a complete understanding of active nematics therefore, this chapter also highlights experimental examples of collective behaviour in active nematics. In particular, we highlight collective behaviour of cells as a well-studied active system in the lab. One notable experimental study found collective edge migration in a confined monolayer of fibrosarcoma cells [85]. This will be of particular importance in Chapter 4. Using a cell-based modelling approach, we introduce the chiral activity covered in section 1.5.3, and find that the modelling approach taken, faithfully reproduces the edge migration phenomenology from the study.

Chapter 2

Modelling active nematics

2.1 Continuum model

The Beris-Edwards formulation from introduced in Chapter 1 section 1.4.1 lays the foundation for the continuum model for an active model system. The model used in this thesis numerically solves the coupled nematohydrodynamic equations from 1.9 and 1.10 and the velocity field $\mathbf{u}$. Work in this thesis is focused on the behavior of an active model system in the presence of strong hydrodynamic screening, and thus we employ equations of dry active nematics [19] with the additional quadrupolar active forces. This means there is no hydrodynamic contribution and the viscous stresses are completely dominated by the frictional dampening ie., $\Pi_{ij}^{\text{Viscous}} = 0$ in the active stress from equation 1.15. Additionally, the passive contribution, also known as 'back-flow' is usually small compared to other stress contributions [74] and will therefore be neglected ($\Pi_{ij}^{\text{Passive}} = 0$). The stress tensor is thereby defined solely by the active contribution

$$\Pi_{ij} = \Pi_{ij}^{\text{Active}}. \tag{2.1}$$

As force is the divergence of the stress tensor from equation 1.9 and including the quadrupolar contribution from equation 1.20, we can express the force as

$$F_i^{\text{Active}} = -\zeta_1 \ \partial_j Q_{ij} - \zeta_2 Q_{ij} \partial_k Q_{kj}. \tag{2.2}$$

In order to find the velocity, we set up a simple force balance equation from equation (1.9). Many dry active systems are in the low Reynolds number regime, we thereby lose the time-dependency and the left-hand side of the equation becomes negligible. The force balance equation thereby simplifies to

$$\partial_j \Pi_{ij} - f u_i = 0. \tag{2.3}$$

The first term, the divergence of the stress tensor $\partial_j \Pi_{ij}$, becomes the force vector from equation 2.2, which yields the following expression for velocity

$$u_i = \frac{1}{f} \left[-\zeta_1 \partial_j Q_{ij} - \zeta_2 Q_{ij} \partial_k Q_{kj} \right]. \tag{2.4}$$

f is the friction coefficient, and ζ_1 and ζ_2 show the activity coefficient related to a force dipole and a force quadrupole, respectively. The two well-known classes of active suspensions, namely extensile and contractile systems, are described by $\zeta_1 > 0$ and $\zeta_1 < 0$, respectively [74]. We study the role of the quadrupole active force in the dynamics of the system by numerically solving the coupled equations of the nematic tensor $\mathbf{Q}$ and the velocity field $\boldsymbol{u}$.

In this regard, we fix the value of the dipolar active force to $\zeta_1 = 0.2$, and study the role of the tumbling parameter χ as well as the strength of the active force quadrupole ζ_2 in the dynamics. As such, we vary the strength of the active quadrupole term in the range $-0.3 \leq \zeta_2 \leq 0.25$, effectively exploring the interplay between the dimensionless ratio $\mathcal{Z} = \zeta_2/\zeta_1$ and the tumbling parameter χ. The system size of 512×512 grid points is simulated with periodic boundary conditions on all sides. Parameters for the rotational diffusivity, regularisation, and friction are fixed at $\Gamma = 0.05$, $g = 0.1$, and $f = 10$. In addition, the elasticity, and the bulk nematic alignment coefficient are set to $\mathrm{K} = 0.15$ and $\mathrm{A} = 0.5$.

2.2 Phase-field model

Phase-field models are used to solve inter-facial problems, and their application to solve single cells problems have been frequent [6]. The model works by introducing a phase-field order parameter ϕ, which is coupled to the nematic behaviour. This allows us to distinguish between active and passive regions. Fig 2.1 shows this distinction with the phase-field having a smooth interface between the two values $\phi = 1$ and $\phi = 0$ of the field. By assigning each cell by a phase-field parameter, the method allows for modelling different cell systems, such as a dense cell monolayer.

2.2.1 Phase-field model for dense monolayer

As stated in section 1.2, cells display properties of active nematics, specifically the formation of topological defects. In cellular monolayers, these defects have been known to control the death and extrusion of Madin-Darby Canine Kidney (MDCK) cells [67]. This is non-trivial as such epithelial cells on a substrate have an isotropic shape and a well defined direction of motion. In that respect, it has been shown that, in dense cellular monolayers, a dipolar interaction based on the cells' deformation leads to symmetry breaking which drives the system out of equilibrium [55].

The active chiral stress is introduced to a dense cellular monolayer using a multiphase-field modelling approach in which each cell i is defined by a phase field $\phi_i(\boldsymbol{x}, t)$ that is advected by the cell velocity $\boldsymbol{v}_i(\boldsymbol{x}, t)$ according to the equation of motion

$$\partial_t \phi_i + \boldsymbol{v}_i(x)\phi_i = -\frac{\delta \mathcal{F}}{\delta \phi_i}. \tag{2.5}$$

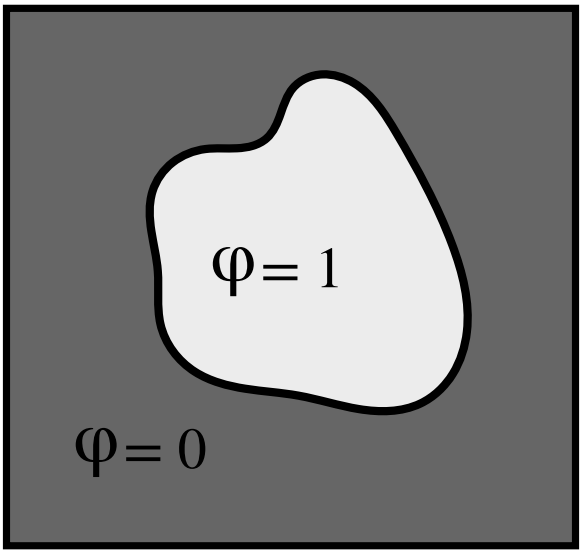

Figure 2.1: Basic schematic of the two different values of ϕ in the phase field.

$\mathcal{F}$ is the free energy describing the individual dynamics on the interface. It is defined as the sum of several contributions, $\mathcal{F} = \mathcal{F}_{\mathrm{CH}} + \mathcal{F}_{\mathrm{area}} + \mathcal{F}_{\mathrm{rep}} + \mathcal{F}_{\mathrm{adh}}$. $\mathcal{F}_{\mathrm{CH}}$ is the Cahn-Hillard free energy which stabilises the cellular interface and is defined as [55, 86]

$$\mathcal{F}_{\mathrm{CH}} = \sum_i \frac{\gamma}{\lambda} \int \mathrm{d}\boldsymbol{x} \left\{ 4\phi_i^2 (1-\phi_i)^2 + \lambda^2 (\nabla \phi_i)^2 \right\}.$$

Here the parameter γ sets the relaxation timescale of shape deformations of individual cells. λ is the corresponding width of the interface at equilibrium for the chosen normalization. $\mathcal{F}_{\mathrm{area}}$ ensures that the cells are only weakly compressible by putting a soft constraint on the cellular area and is given by

$$\mathcal{F}_{\mathrm{area}} = \sum_i \mu \Big(1 - \frac{1}{\pi R^2} \int \mathrm{d}\boldsymbol{x}\, \phi_i^2 \Big)^2,$$

where R is the individual cell radius and μ is a parameter set to the time scale of area changes, which makes the target area of each cell πR^2 [55, 86]. The passive contributions come in the form of repulsive and adhesive forces. The term $\mathcal{F}_{\mathrm{rep}}$ is a passive contribution to the free energy which penalises overlaps between neighboring cells [55, 86],

$$\mathcal{F}_{\mathrm{rep}} = \sum_i \sum_{j \neq i} \frac{\kappa}{\lambda} \int \mathrm{d}\boldsymbol{x}\, \phi_i^2 \phi_j^2$$

The parameter κ sets the strength of the repulsive forces. Finally, the free energy of cell-cell adhesion is calculated as

$$\mathcal{F}_{\mathrm{adh}} = \sum_i \sum_{j \neq i} \omega\lambda \int \mathrm{d}\boldsymbol{x}\, \nabla\phi_i \cdot \nabla\phi_j$$

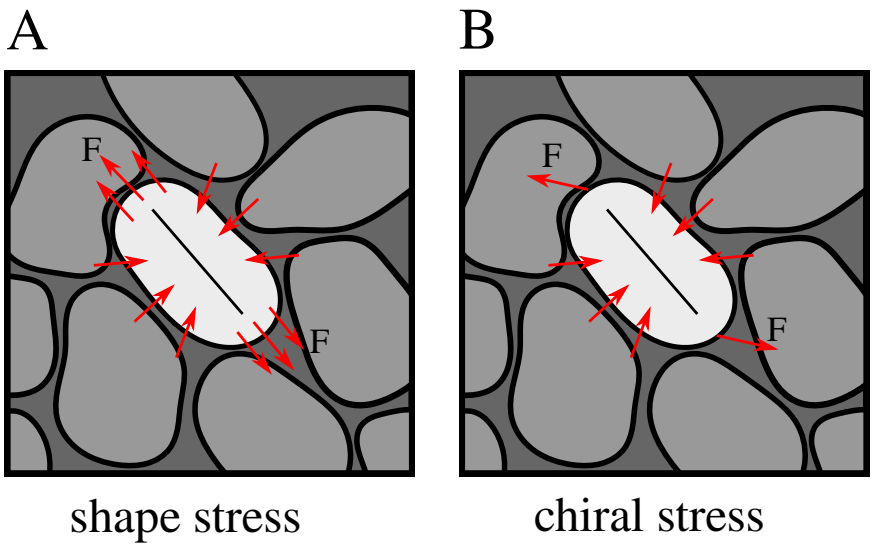

Figure 2.2: Schematic of the distribution of forces for A) achiral and B) chiral active stress. The red arrows correspond to active forces. For the achiral case, the direction of the force is parallel to the primary deformation axis with external inwards deformation being applied by contact with neighboring cells. In contrast, the chiral stress appears when the force exerted by a cell is neither perpendicular nor parallel to the cells alignment axis.

Here ω is the parameter that controls the relaxation of adhesive forces and determines the strength of cell-cell adhesion. The regularisation of the adhesive interaction is defined in the rightmost fraction in the derivative of the free energy $\mathcal{F}_{\mathrm{adh}}$

$$\frac{\delta \mathcal{F}_{\mathrm{adh}}}{\phi_i} = \frac{\mathcal{F}^0_{\mathrm{adh}}}{\delta \phi_i} \frac{1}{\sqrt{1 + \left(\sum_{\mathrm{j}\neq \mathrm{i}} \nabla^2 \phi_i\right)^2}}, \tag{2.6}$$

where

$$\mathcal{F}^0_{\mathrm{adh}} = 2 \sum_i \sum_{j \neq i} \omega \lambda \int \mathrm{d}\boldsymbol{x}\, \nabla \phi_i \cdot \nabla \phi_j \tag{2.7}$$

[47]. As cells are considered to be in the low-Reynolds-number regime, we have overdamped dynamics and thus the force acting on velocity reduces to

$$\xi \boldsymbol{v}_i = \boldsymbol{f}_i^{\mathrm{tot}}, \tag{2.8}$$

where ξ is a substrate friction coefficient and $\boldsymbol{f}_i^{\mathrm{tot}}$ is the sum total of the different force contributions, $\boldsymbol{f}_i^{\mathrm{tot}} = \boldsymbol{f}_i^{\mathrm{passive}} + \boldsymbol{f}_i^{\mathrm{pol}} + \boldsymbol{f}_i^{\mathrm{int}}$, $\boldsymbol{f}_i^{\mathrm{passive}}$ is the passive thermodynamic force that drives a non-equilibrium cell towards a lower free energy state, while $\boldsymbol{f}_i^{\mathrm{pol}}$ represents the force acting on an individual cell due to filament treadmilling. Finally, the active inter-cellular force, $\boldsymbol{f}_i^{\mathrm{int}}$, is defined by the inter-celluar forces driven by the deformation of the individual cell.

To demonstrate the effect of a chiral stress, it is possible to define the interface forces in terms of a macroscopic tissue stress tensor σ_{tissue}:

$$\boldsymbol{f}_i^{\text{int}} = \int \mathrm{d}\boldsymbol{x}\phi_i \nabla \cdot \sigma_{\text{tissue}} = -\int \mathrm{d}\boldsymbol{x}\ \sigma_{\text{tissue}} \cdot \nabla\phi_i. \tag{2.9}$$

We define the active stress tensor σ_{tissue} by including the chiral activity expression derived by Hoffmann et al. [36] in addition to the active forces based on shape deformation

$$\sigma_{\text{tissue }ij} = -\zeta_S Q_{ij} - \zeta_{\text{chiral}} \epsilon_{ik}\ Q_{kj}, \tag{2.10}$$

where the subscripts refer to tensor components in a Cartesian basis, ϵ_{ik} is the two-dimensional Levi-Civita tensor ($\epsilon_{xx} = \epsilon_{yy} = 0, \epsilon_{xy} = 1, \epsilon_{yx} = -1$), ζ_S and ζ_{chiral} are the activity coefficients of shape deformation and chirality respectively and Q is the nematic tensor $Q = \sum_i \phi_i \mathbf{S_i}$ with $\mathbf{S_i}$ being the deformation tensor of cell i defined as

$$\mathbf{S}_i = -\int \mathrm{d}\boldsymbol{x} \left[\nabla\phi_i \nabla\phi_i^T - \frac{1}{2}\mathrm{Tr}(\nabla\phi_i \nabla\phi_i^T)\right], \tag{2.11}$$

following [86]. As both ζ_S and ζ_{chiral} correspond to stresses of shape deformation, it is important to highlight that ζ_S and ζ_{chiral} are the coefficients of respectively achiral and chiral shape-deformation-driven activity.

Chapter 3

Quadrupolar active stress induces exotic phases of defect motion in active nematics

A wide range of living and artificial active matter exists in close contact with substrates and under strong confinement, where in addition to dipolar active stresses, quadrupolar active stresses can become important. Here, we numerically investigate the impact of quadrupolar non-equilibrium stresses on the emergent patterns of self-organisation in non-momentum conserving active nematics. The results reveal that beyond having stabilising effects, the quadrupolar active forces can induce various modes of topological defect motion in active nematics. In particular, we find the emergence of both polar and nematic ordering of the defects, as well as new phases of self-organisation that comprise topological defect chains and topological defect asters. The results contribute to further understanding of emergent patterns of collective motion and non-equilibrium self-organisation in active matter. This chapter closely follows the authored publication [72].

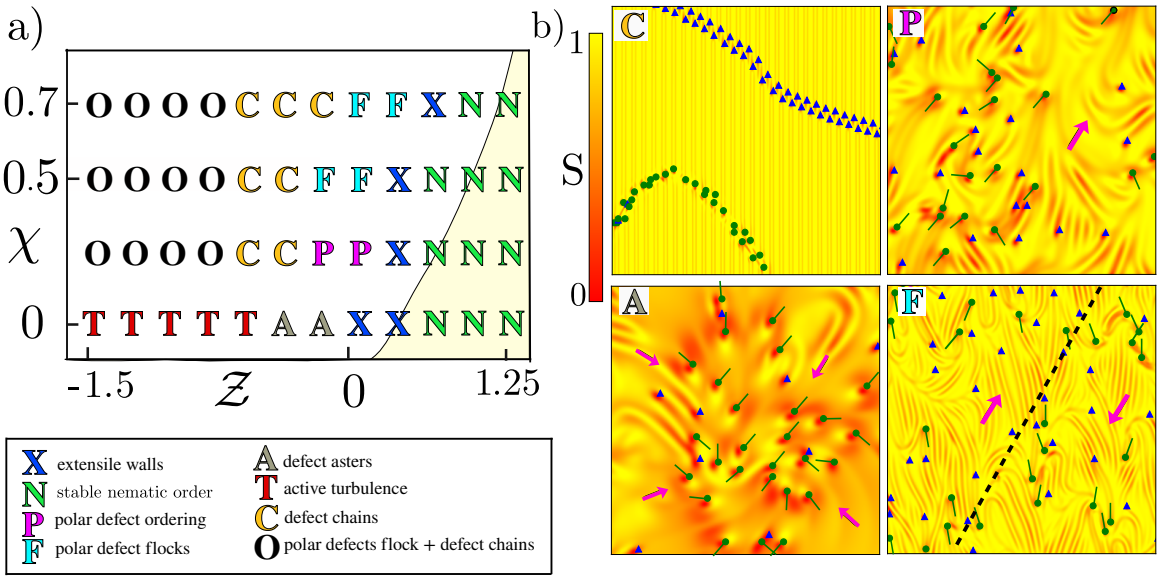

Figure 3.1: a) Phase space of the system for different values of the aligning parameter χ and the activity ratio $\mathcal{Z} = \zeta_2/\zeta_1$. The nematic order can become stable for positive values of the force quadrupole term. The yellow region in the phase diagram shows the stable region found analytically in [48]. b) Snapshots showing the distinguishable characterization of defect chains, polar defect ordering, defect asters and polar defect flocks. The underlying color map shows the magnitude of the nematic order S, and $+1/2$ $(-1/2)$ defects are represented in green (blue). In the snapshots, arrows show the direction of the motion of $+1/2$ defects and dashed lines separate regions with different orientations of the $+1/2$ defects.

3.1 Introduction

Chapter 1 section 1.5.1 covered how the force dipole represents the force exerted by a single active particle. Depending on force dipole coefficient ζ_1, these particles can be considered 'pullers' or 'pushers' (see Fig. 1.6.A/.B). In addition to this well-established dipolar activity, the force distribution of the higher angular symmetry, the force quadrupole term with coefficient ζ_2 in equation. 2.2, becomes important in systems in contact with a substrate, where the momentum is not conserved [48]. These systems, known as dry active matter systems, were covered in Chapter 1 section 1.2.2. Descriptions based on dry active matter theories have been helpful in investigating the different patterns in clusters of bacteria which live on dry surfaces in tight spaces [63, 32]. Since in this work our focus is on the behavior of active model systems in the presence of strong hydrodynamic screening, we employ equations of dry active nematics [19] with the additional quadrupolar active forces. The active nematic model is chosen since it has proven successful in describing a wide variety of active materials that constitute elongated building blocks such as rod-shaped bacteria [56],

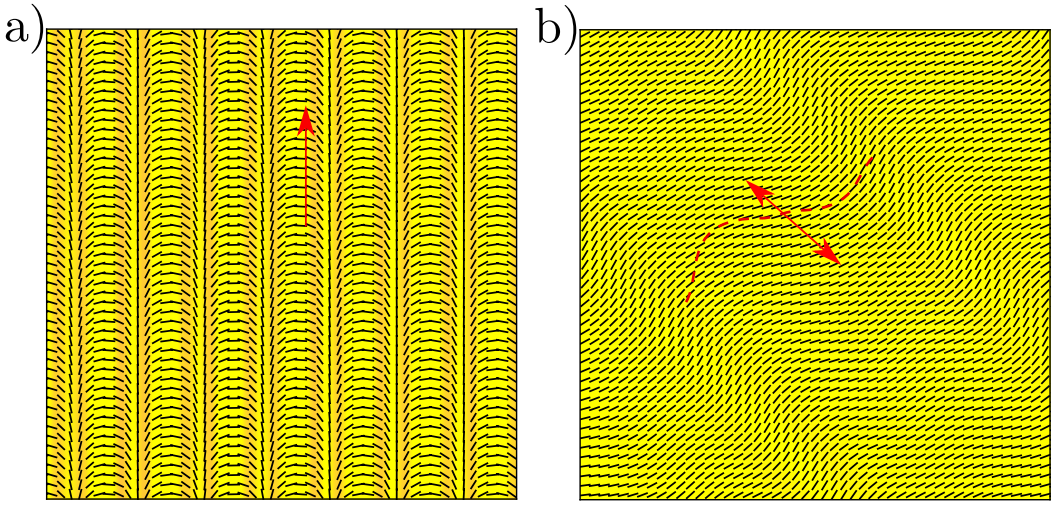

Figure 3.2: a) and b) show arches and walls, respectively. Arches have a polar symmetry (red arrow), whereas walls have a nematic symmetry (red double headed arrow). Red dashed line shows a bend deformation in walls.

subcellular filaments [4], and spindle-shaped cells [24], as well as deformable cells in which orientational ordering is an emergent feature [55, 67, 11].

In order to investigate the effects of the quadrupolar contribution, we employ the continuum model introduced in Chapter 2 section 2.1 to study a dry active system. Using the parameters stated in section 2.1, we start by doing a parametric scan of the interplay between the dimensionless ratio $\mathcal{Z} = \zeta_2/\zeta_1$ and the tumbling parameter χ. With the goal of creating a phase-diagram to map out all the evolution behaviour from the different simulations, we take different quantitative measures to distinguish between the different phases of self-organisation. These measures include global quantitative analysis to quantify the overall impact of the quadrupolar activity, as well as local analysis to quantify the behaviour of topological defects.

3.1.1 Stability diagram

We begin by investigating the emergent patterns for varying values of the quadrupolar to dipolar activity ratio $\mathcal{Z} = \zeta_2/\zeta_1$ and the flow-aligning parameter χ. The results are summarised in a stability diagram in Fig 3.1, where distinct patterns of motion are represented. In what follows, we refer to defect-less nematic phases as "stable nematic phases". In the stable nematic phase (in contrast to the unstable nematic phase) we observe perfect nematic order without any defects.

Fig. 3.1 shows that a positive value of the quadrupolar activity can stabilise the nematic phase and the required quadrupolar force for stability increases with increasing the value of the flow-aligning parameter. This is in agreement with the analytical result of [48]: in

Fig 3.1 we show the stable nematic phase predicted analytically in yellow background color. Note that the analytical boundary of the stable phase has been found by linearising the dynamical equations. However, in our simulations we solve the full nonlinear equations and as a result we do not expect a perfect match.

At the border between stable nematic phase and unstable phases, flows induced by dipolar activity are just strong enough to trigger nematic deformations but not strong enough to nucleate topological defects and instead we observe the formation of *extensile walls*. These extensile walls have also been observed previously [58] in wet active nematics in the presence of friction, and are a consequence of the competition between active forces to create defects and elastic forces to maintain the nematic phase. The walls consist of periodic bend deformation of the director and have a nematic symmetry along an axis (see Fig. 3.2 (b)). For larger values of activity, these bend deformations grow and form defects. Fig. 3.2 (a) also shows that, in contrast to walls which have a nematic symmetry, arches have a polar symmetry. The arches consist of both bend and splay deformation. It has been shown in a previous study (Ref. [58]) that arches are steady state solutions of the nematohydrodynamic equations, even in the absence of the quadrupolar activity, when friction is larger than a critical value. Arches do not have a length, but when they form they evolve towards a uniform size.

Going beyond the stability boundary, topological defects are nucleated in the system and we observe the emergence of several dynamic phases of defect organisation as a result of the competition between dipolar and quadrupolar active forces.

To quantitatively distinguish between the stable phase (Fig 3.1, *yellow region*), where we either observe a nematic phase or extensile walls, and an unstable phase, where topological defects form and patterns emerge, we calculate the root-mean-square velocity averaged over both space and time after the statistical steady-state is reached. As evident from Fig 3.3.a active flows decrease with increasing the quadrupolar force coefficient ζ_2, which is consistent with the stabilising effect of the quadrupolar term. The development of active turbulence stems from the onset of instabilities in the director field. Parallel walls consisting of lines of bend deformation separate the nematic regions. The decay of these walls leads to the formation of topological defects [76]. In order to quantify the nematic order and distinguish the nematic phase, we measure the average magnitude of the nematic order (defined as $S_0 = \langle Q_{xx}^2 + Q_{yx}^2 \rangle$). This quantity measures the global nematic order and thus indicates the overall stability of the nematic phase. A decrease in the value of the nematic order indicates the formation and presence of more defects. The average order is shown in Fig. 3.3b for different values of the tumbling parameter. These graphs show the same trend as the average mean root square velocity graphs, indicating that flows are mainly created in places with large drop in the magnitude of the nematic order. Both the graphs in Fig. 3.3a and Fig. 3.3b show a transition from the disordered phase to ordered phase by increasing the quadrupole force.

To further distinguish between the ordered and disordered phases of defect configurations we measure the average deformation, defined as $\langle \Delta n \rangle = \langle (\partial_i \partial_j Q_{ij})^2 \rangle$, for different values of the tumbling parameter and as a function of activity ratio $\mathcal{Z}$. A large value of deformation

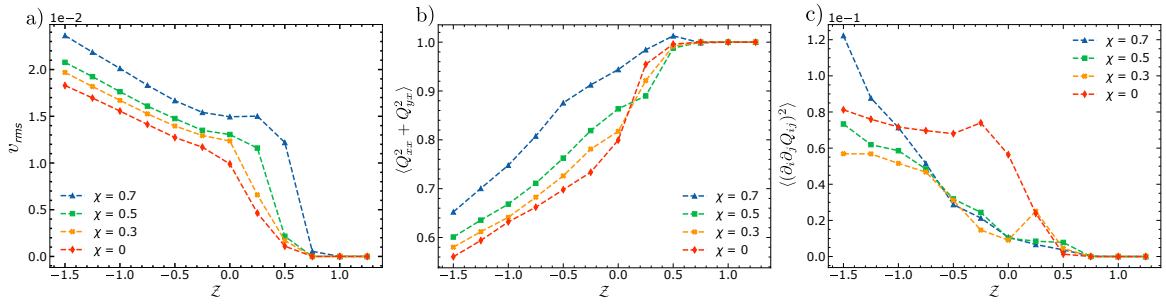

Figure 3.3: a) Root mean square velocity $v_{\rm rms}$ averaged over space and time in steady state. Regardless of the aligning parameter $v_{\rm rms}$ decreases as $\mathcal{Z}$ increases. By proxy, it is also apparent that increasing the quadrupolar active term, lowers the energy of the system. b) Magnitude of the nematic order defined as $\langle Q_{xx}^2 + Q_{yx}^2 \rangle$ averaged over space and time in steady state. The average order follows the inverse trend compared to the rms-velocity, and increases by increasing $\mathcal{Z}$. c) Average deformation defined as $\langle \Delta n \rangle = \langle (\partial_i \partial_j Q_{ij})^2 \rangle$. The average is taken over time and space in steady state. The fall in deformation correlates with observed stabilisation as a consequence of increasing $\mathcal{Z}$.

follows a distortion in **Q**-tensor. Note that this quantity is different from the average order S_0 as it accounts for the distortions in the director and the deviation from the global nematic ordered phase. $\langle \Delta n \rangle$ is maximum in the presence of walls or in the active turbulence phase, as in these phases the global distortions in the director is maximum. The average distortion is presented in Fig. 3.3c for varying values of the tumbling parameter. Note that ordered phases of defect organisation do not correspond to a peak in the distortion graph as in these phases the distortions in the director are local (in places of defects) and not global.

Next, we describe the characteristics of defect self-organisation as this new non-linear regime is the focus of the current study.

3.1.2 Dynamic phases

We now turn to the unstable part of the phase diagram, where for a given value of the flow-aligning parameter, the instability driven by dipolar activity is strong enough to lead to deformation of the director field and nucleation of topological defects, while the presence of the quadrupolar activity acts to restructure the spatial defect organisation. In this regime, we found a variety of phases depending on the value of the tumbling parameter:

Defects flocking: In the unstable phase, but close to the boundary of the stable phase, we observe a phase in which different groups of self-propelled +1/2 defects move together forming flocks of motile topological defects (Fig. 3.1 and Supplementary Movie 1 in [1]). Fig. 3.6a shows the angular distribution of +1/2 defects within this phase. Defects are identified using the diffusive charge density [12]

$$s = \left(\frac{1}{2\pi}\right) \times \left(\left[\frac{\partial Q_{xx}}{\partial x} \frac{\partial Q_{xy}}{\partial y} \right] - \left[\frac{\partial Q_{xx}}{\partial y} \frac{\partial Q_{xy}}{\partial x} \right] \right) \tag{3.1}$$

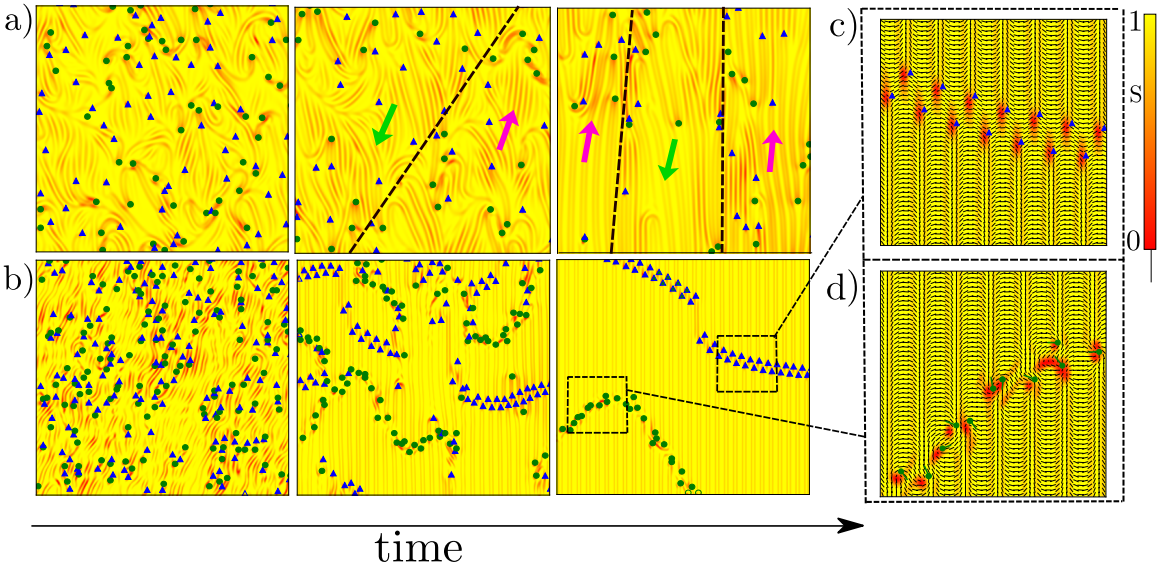

Figure 3.4: Time evolution of dynamics for (a) polar defect flock and (b) defect chains. In the polar defect flocking phase, the system forms motile defects that flock together in anti-parallel directions as indicated by the arrows. Defects in the chain phase self-organise to form (c) long chains of robust $-1/2$ defects as well as (d) chains of dynamic oscillating $+1/2$ defects as the system relaxes towards a steady state. In the snapshots, arrows show the direction of the motion of $+1/2$ defects and dashed lines separate regions with different orientations of the $+1/2$ defects. Here, we have used $\zeta_2 = 0, \chi = 0.7$ for the chain phase and $\zeta_2 = 0.05, \chi = 0.3$ for the polar phase.

which takes values of $\pm 1/2$ at the defect cores and is zero otherwise. The angle θ is calculated using $\nabla \cdot \mathbf{Q} = (\cos\theta, \sin\theta)$, where $\nabla \cdot \mathbf{Q}$ gives the direction of the defects self-propulsion [61] that for extensile systems ($\zeta_1 > 0$) is from tail to head of the $+1/2$ defect. Interestingly, in this phase, the defects in each flock move in the same direction and show polar order, but different defect flocks can migrate in anti-parallel directions within the system as seen from the snapshots in Fig. 3.4a. To show this behavior more clearly, we calculate both polar and nematic order parameter for the alignment of the $+1/2$ topological defects. The polar ordering is defined by

$$P_{+1/2} = \sqrt{P_x^2 + P_y^2}, \tag{3.2}$$

where

$$[P_x, P_y] = \left[\sum_i^N \frac{m_{xi}}{N}, \sum_i^N \frac{m_{yi}}{N}\right], \tag{3.3}$$

and m is defined by the orientational angle θ_i of each $+1/2$ defect as $m_{xi} = \cos\theta_i$ and $m_{yi} = \sin\theta_i$. Similarly, the nematic order of the defect alignment is characterised by the

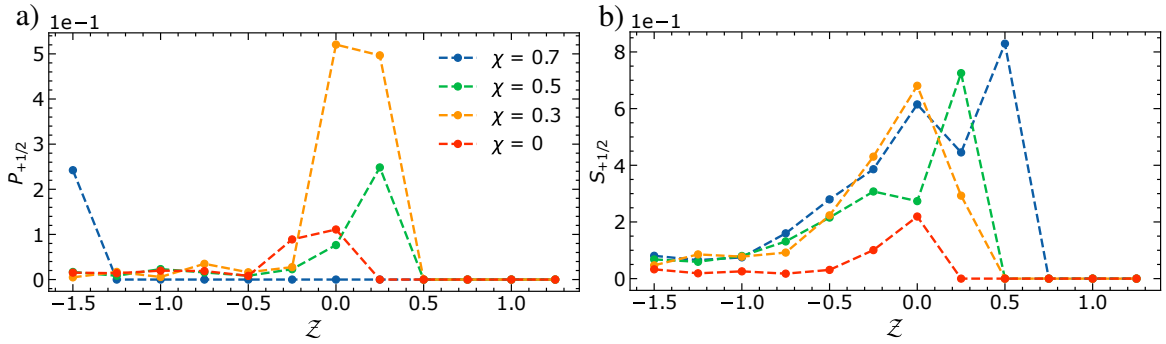

Figure 3.5: a) Screening of polar ordering $P_{+1/2}$ (equation 3.2) shows peaks for the aligning $\chi = 0.3$. These peaks correspond to the phase with polar ordering of defects. b) Plot of the nematic ordering of defect alignment (equation 3.4). The peaks correspond to the observed polar flocks and defect chains which show nematic orientations of their $+1/2$ defects.

higher order multipole of the alignment angle [18], $S_{+1/2} = \sqrt{N_1^2 + N_2^2}$, where

$$[N_1, N_2] = \frac{1}{N} \sum_{i}^{N} (\cos 2\theta_i, \sin 2\theta_i). \tag{3.4}$$

For a perfect polar alignment of the motile defects $P_{+1/2} = 1.0$, while for the perfect nematic alignment $S_{+1/2} = 1.0$. For the angular distribution represented in Fig. 3.6a that corresponds to the defects flocking state, we find $P_{+1/2} = 0.24$ and $S_{+1/2} = 0.8$, indicating that the orientational organisation of the $+1/2$ defects in the defect flocks state shows a dominant nematic alignment. See Fig. 3.5 for the full screening of $P_{+1/2}$ and $S_{+1/2}$

Polar defect ordering: Close to the defect flocking state, reducing the flow-aligning parameter together with lower quadrupolar activity leads to the global polar ordering of the motile $+1/2$ defects (Fig. 3.1 and Supplementary Movie 2 in [1]). This is reminiscent of the polar defect ordering predicted by the hydrodynamic theory of active defects in the over-damped limit and is due to the active aligning torque on defects in a charge neutral system [69]. The polar ordering state is best represented in the angular distribution plot showing the sharp peak in the orientational alignment of the defects (Fig. 3.6b) and corresponds to the quantitative value of the global polar order $P_{+1/2} = 0.5$ (Fig. 3.5a).

Defect asters and active turbulence: At the zero value of the flow-aligning parameter, where the director only responds to the rotational part of the flow gradient, and for negligible values of the quadrupolar activity coefficient, we find a different state characterised by aster-like organisation of groups of $+1/2$ defects (Fig. 3.1 and Supplementary Movie 3 in [1]). Increasing the strength of the quadrupolar activity towards negative values results in the breakup of the aster-like structures and the establishment of the active turbulence characterised by the chaotic motion of the topological defects (see Supplementary

Movie 4 in [1]). Within both phases the orientational organisation of the defects is isotropic (Fig. 3.6c,d).

Defect chains: Interestingly, for negative moderate quadrupolar activities, we found a phase in which $\pm 1/2$ defects self-organise into large chain-like structures. The chains of $+1/2$ and $-1/2$ defects show different characteristics: while $-1/2$ defect chains are stable and do not restructure after they are formed, the $+1/2$ defect chains are dynamic and within the chains pairs of $\pm 1/2$ defects nucleate, annihilate, move, and oscillate around each other (see Fig. 3.4b and Supplementary Movie 5 in [1]) in a fashion resembling local defect dancing that has been reported for confined active nematics [22]. The large-scale defect chains could be reminiscent of the propagating soliton-like clusters that have been recently discovered for confined active nematics with chiral anchoring [46], though here they are emergent properties of the system, where neither confinement nor chiral anchoring are present. In this vein, the impact of the friction on hydrodynamic screening and quadrupolar activity on breaking the angular momentum conservation could resemble the confinements and chiral anchoring effects, respectively, that have been shown to induce soliton-like defect clusters.

In order to better understand the mechanism of chain formation we analytically calculate the force induced by dipolar and quadrupolar activities around isolated $\pm 1/2$ topological defects. The $\mathbf{Q}$ tensor around a topological defect with charge k reads:

$$\mathbf{Q} = \begin{pmatrix} \cos(2k\phi) & \sin(2k\phi) \\ -\sin(2k\phi) & \cos(2k\phi) \end{pmatrix}, \tag{3.5}$$

where the defect symmetry axis is along the x-axis (as represented in Fig. 3.8), and ϕ is the polar angle (measured counter-clockwise with respect to the x-axis). Using this definition for the $\mathbf{Q}$ tensor the active force around a defect reads:

$$\mathbf{f}^a = \frac{qk}{r} \begin{pmatrix} \zeta_2 \cos\phi - \zeta_1 \cos\phi(1-2k) \\ \zeta_2 \sin\phi + \zeta_1 \sin\phi(1-2k) \end{pmatrix}. \tag{3.6}$$

From the symmetry of the quadrupolar active force it is expected that such a force does not have any impact on the self-propulsion speed of the defects. Interestingly, however, the quadrupolar activity induces distinct diverging and converging forces around $+1/2$ and $-1/2$ topological defects, respectively (Fig. 3.8). The converging force around an isolated $-1/2$ defect can explain the attraction of $-1/2$ defect pairs and the formation of chains of $-1/2$ defects (Fig. 3.4b,c). On the other hand, the $+1/2$ defects that are in small distance from the $-1/2$ chain annihilate, but the $+1/2$ defects far from the $-1/2$ chain can form a dynamic chain. The orientation of the defects in a $+1/2$ chain, agrees with the active torque between $+1/2$ defects introduced in Ref. [70]. In Ref. [70] it has been shown that two isolated $+1/2$ defects orient towards each other due to an active torque caused by the dipolar activity. The alignment of two $+1/2$ defects towards each other has indeed been observed in experiments and simulations of active systems in circular confinement where the boundary condition imposes formation of two $+1/2$ defects. In the simulations

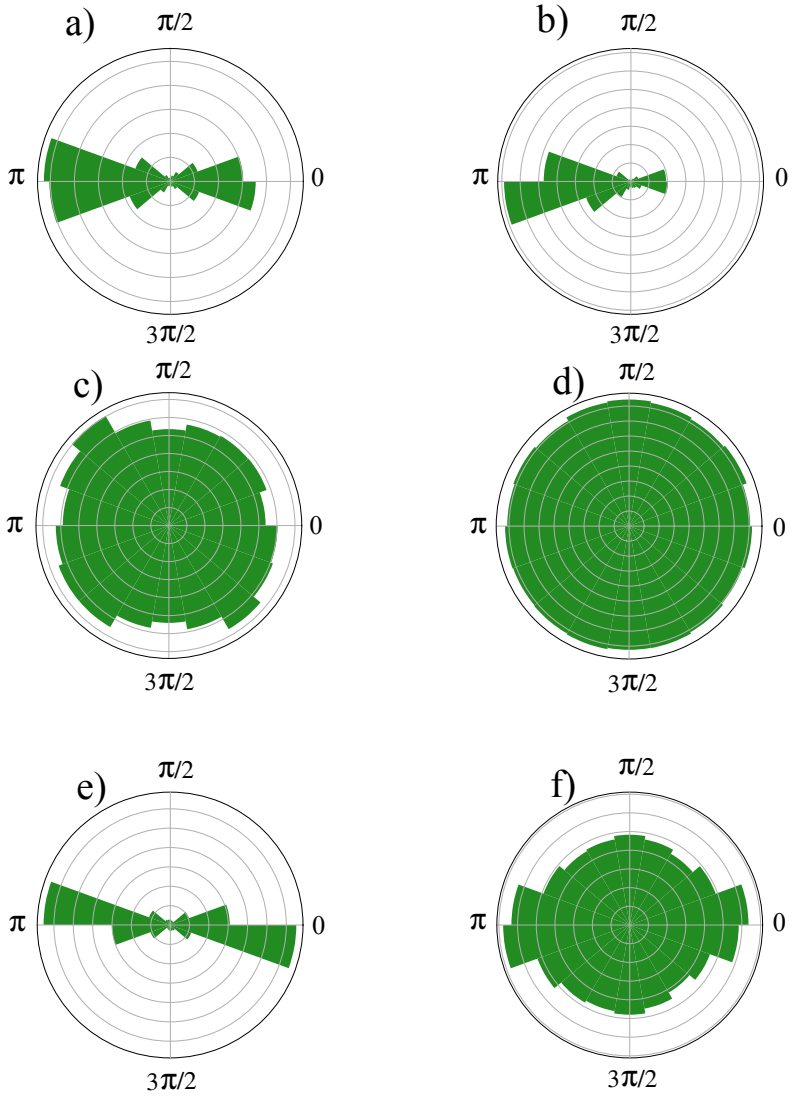

Figure 3.6: Angular distribution of $+1/2$ defects for different phases: a) Defects flocking, b) Polar defect order, c) Active turbulence, d) Defect asters, e) Defect chain and f) Polar defect flock coexisting with the defect chain. The different phases are distinguishable both by the direction of the $+1/2$ defects as well as the number of defects that form in a given phase. The colour bar corresponds to the number of $+1/2$ defects orientated at angle θ Here, we have used the following parameter values: chains ($\zeta 2 = 0, \chi = 0.7$), polar ($\zeta_2 = 0.05, \chi = 0.3$), asters ($\zeta 2 = -0.05, \chi = 0$), polar flock ($\zeta_2 = 0.05, \chi = 0.5$), coexistence of polar flock and chains ($\zeta_2 = -0.15, \chi = 0.3$), turbulence ($\zeta_2 = -0.25, \chi = 0$).

in bulk, however, this has not been observed, mainly because the topological charge in bulk simulations is zero and so $+1/2$ defects are not isolated due to the presence of -1/2 defects.

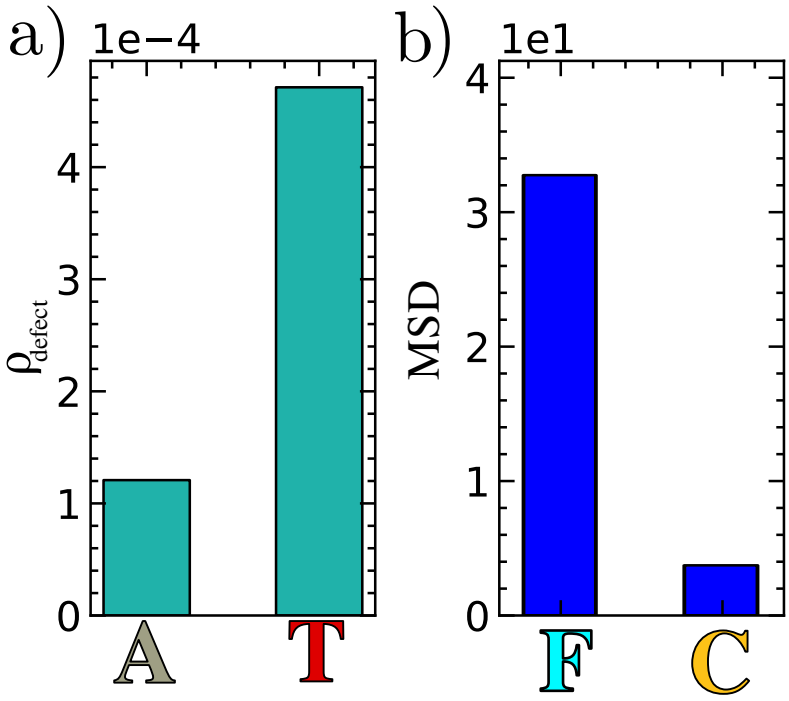

Figure 3.7: Comparative plots to further distinguish phases that have a similar angular distribution of $+1/2$ defect. a) Defect density ρ_{defect} comparing the aster phase and turbulent phase. The abundance of defects is a characteristic of active turbulence. b) Mean squared displacement (MSD) of $-1/2$ defects. In the chain phase, defects form long dormant chain-like structures. In contrast, the defect flocking phase is characterised by flocks of topological defects in motion.

In our simulations, since the new active force aggregates $-1/2$ defects, $+1/2$ defects that are far from the $-1/2$ defect chain can experience the active torque, and so orient towards each other. Their self-propulsion velocity (which is towards their head) then makes their position stable.

Finally, parameter-wise deep in the unstable phase we found a phase in which the polar defect flock phase coexists with the defect chain phase. In both pure defect chain phase and the coexistence phase, characterisation of the angular defect orientation reveals a dominant nematic alignment of the $+1/2$ defects (Fig. 3.6e, f). In summary, to distinguish between different phases, we note that in the "stable nematic phase" and "extensile walls", no defects form and so this distinguishes these two phases from the other phases. Then looking at $\langle \Delta n \rangle$, can distinguish between walls and stable nematic order, as this quantity is large (zero) for the former (latter). The polar defect phase is then distinguished from the other phases by looking at the distribution of the $+1/2$ defect orientation (Fig 3.6.b) as this is the only phase with a polar symmetry in the distribution. Then, "defect flocks" and "defect chain" phases can be distinguished from other phases by looking at the orientation of defects

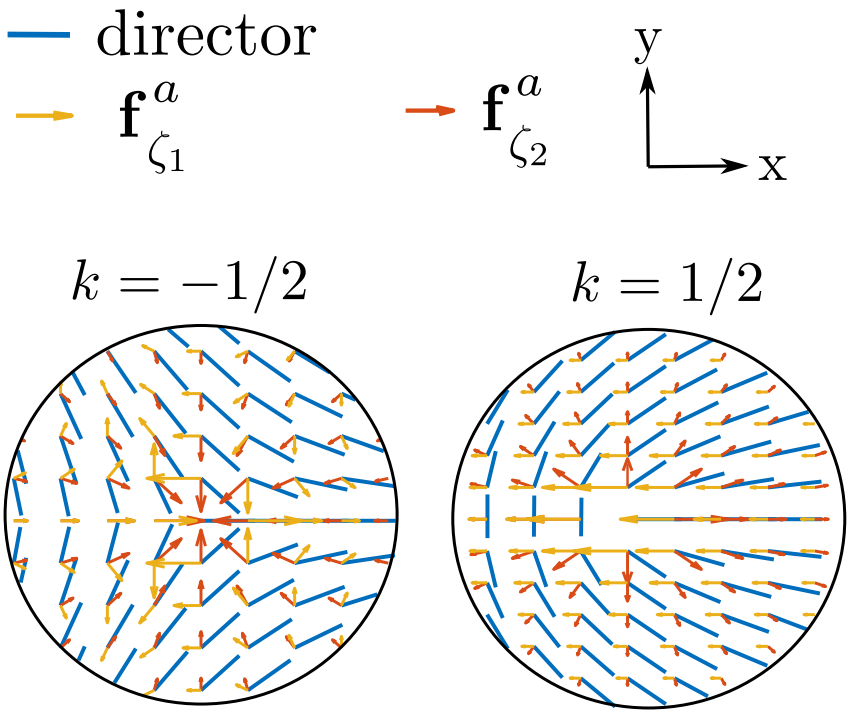

Figure 3.8: Force distribution around $\pm 1/2$ topological defects due to the dipolar and quadrupolar active forces, showing distinct diverging and converging force patterns due to the quadrupolar force around $+1/2$ and $-1/2$ defects, respectively. Here, blue solid lines indicate the director field of the defects, while yellow and red arrows illustrate force induced by dipolar and quadrupolar activities, respectively. Here, we have used $\mathcal{Z} = -0.75$.

(Fig 3.6.a and e) which show a nematic symmetry in both of these phases. To distinguish these two phases from each other, we have now plotted the mean square displacement of -1 defects. Chain phases have ordered and stable $-1/2$ defects, on the other hand, the dynamics of the polar flock phase has both $+1/2$ and $-1/2$ defects in motion and thus a similar mean squared displacement MSD for both defect types (Fig. 3.7,b).

Finally, both the "aster" phase and "active turbulence" phase have an isotropic distribution of defect orientation and this distinguishes them from the other phases. The distinction between these two phases can be done by looking at the defect density ρ_{defect} which is much higher in the active turbulence phase (Fig. 3.7,a).

3.2 Conclusion

We have numerically studied the dynamics of active nematic systems in contact with a substrate. In this setup, a new active force contribution, that is absent in a bulk momentum conserving system, plays a role in the dynamics of the system [48]. We confirmed that for one sign of this active force, the nematic state becomes stable in agreement with the analytical result of Ref. [48]. Remarkably, going beyond linear stability, we also showed that in the unstable regime where the new active force cannot recover the nematic phase, it introduces new patterns of topological defect organisation in the system. In particular, we found the formation of stable chains of $-1/2$ topological defects, while the corresponding $+1/2$ defects form elongated clusters and oscillate around a center in pairs. By varying the aligning parameter, we additionally found the emergence of polar defect flocks, in which the system forms different flocks of $+1/2$ defects. Defects in each flock represent polar order but different flocks move in opposite direction and show nematic order. Furthermore, states showing pure polar flocking of the $+1/2$ defects and aster-like dynamic defect configurations, in which $+1/2$ defects point radially towards a center, were uncovered for varying quadrupolar-to-dipolar active force ratios and flow aligning parameters.

This work could supplement further investigations into taming of active turbulence. Moreover, it provides numerical context to both the work in [48] as well as possible experimental assay results in which the quadrupolar force plays a role in the active stabilization or destabilization of the system. The exotic defect organisation phases revealed by the current numerical study can further trigger new experimental exploration of the topological defect structures in strongly confined active nematic systems.

Chapter 4

Active chiral stress induces collective motion in cell monolayers

Recent experiments conducted using human fibrosarcoma cells in confinement have revealed appearance of collective motion of cells by virtue of topological chiral edge currents. In this project we add a chiral stress to a phase-field model and investigate the collective behavior of cells under different numerical conditions. We are able to reproduce the phenomena of chiral edge currents when placed in a domain with boundary walls. These edge currents are shown to be robust and exist in other geometries such as the configurations of channels and rectangular stripes simulated in this work. Finally, local defect analysis reveals the chiral stresses impose a tilt on the flow-field around a $+1/2$ defect. This strengthens experimental results and serves as a precursor for further numerical exploration in the realm of biological organisation in cell monolayers.

4.1 Introduction

Experimental assays on monolayers of spindle-like cells on adhesive stripe-shaped plates have shown convincing results of various collective phenomena in epithelial cells governed by active nematic hydrodynamics. It has further been suggested that some of these unexplored features could be attributed to the presence of chiral stresses over length scales larger than the typical size of a cell [25]. The work of Hoffmann et al. [36] elaborated on this by analytically introducing a chiral stress for a nematic cell monolayer. The authors show that chiral active stresses can cause a misalignment between cell motion and defect polarity as evidenced by a tilt in the flow surrounding $\pm 1/2$ topological defects [36]. Evidence of edge currents, which are collective streams of motion alongside the boundary of a confinement, has been observed in experimental assays using human fibrosarcoma (HT1080) cells in confinement on adhesive stripes. This behaviour was also explained to be governed by the physics of active nematics [85]. Corresponding numerical simulations based on hydrodynamics led to the suggestion that the edge currents were governed by layers of $+1/2$ topological defects, where the defects are anchored at the confining walls and act as local sources of chiral active stress [85].

In order to investigate the effect of the chiral stress on a cellular monolayer, we employ the phase-field model introduced in Chapter 2 Section 2.2 to study the collective behaviour of the entire cellular monolayer in different geometric configurations.

We start with a comparative simulation of the cell monolayers with different types of activity both chiral and non-chiral. We then explore the collective behaviour of the system when different types of boundary conditions are used in simulation of the monolayer. Domains with periodic boundary conditions are compared with hard walls. In addition, the monolayer in channels, which are comprised of hard walls and periodic boundaries, is also investigated. Additionally, the magnitude of the activity coefficients, as well as cell-cell adhesion is also varied. Finally, we investigate the flow-fields around a $+1/2$ defect for a system with achiral and chiral stresses respectively.

4.2 Chiral and achiral stresses

We compare periodic-boundary simulations (box size 256×256) of cell monolayers with only achiral shape-driven stresses ($\zeta_S \neq 0, \zeta_{\text{chiral}} = 0$) to ones with only chiral activity ($\zeta_S = 0, \zeta_{\text{chiral}} \neq 0$). Fig 4.1 shows snapshots of the cellular monolayer as well as the corresponding velocity field for both the shape deformation and chiral activity respectively. The velocity field plots reveal the behavioural changes in the system. The simulation with the chiral stresses has the cells form multiple vortex currents, all at a similar length scale in contrast to the achiral stresses, which creates nematic flow patterns within the monolayer. For these simulations, parameters are set at $\mu = 5$, $= 0.2$, $\lambda = 3$, $\xi = 1$, and $\gamma = 0.2$. Now that the behavioral differences between the chiral and achiral stresses have been established, we turn to investigating the effects of ζ_{chiral}. For this we increase the chiral activity ζ_{chiral} in 8 increments between $\zeta_{\text{chiral}} = 0.0015$ and $\zeta_{\text{chiral}} = 0.0050$. At activities $\zeta_{\text{chiral}} < 0.002$ the

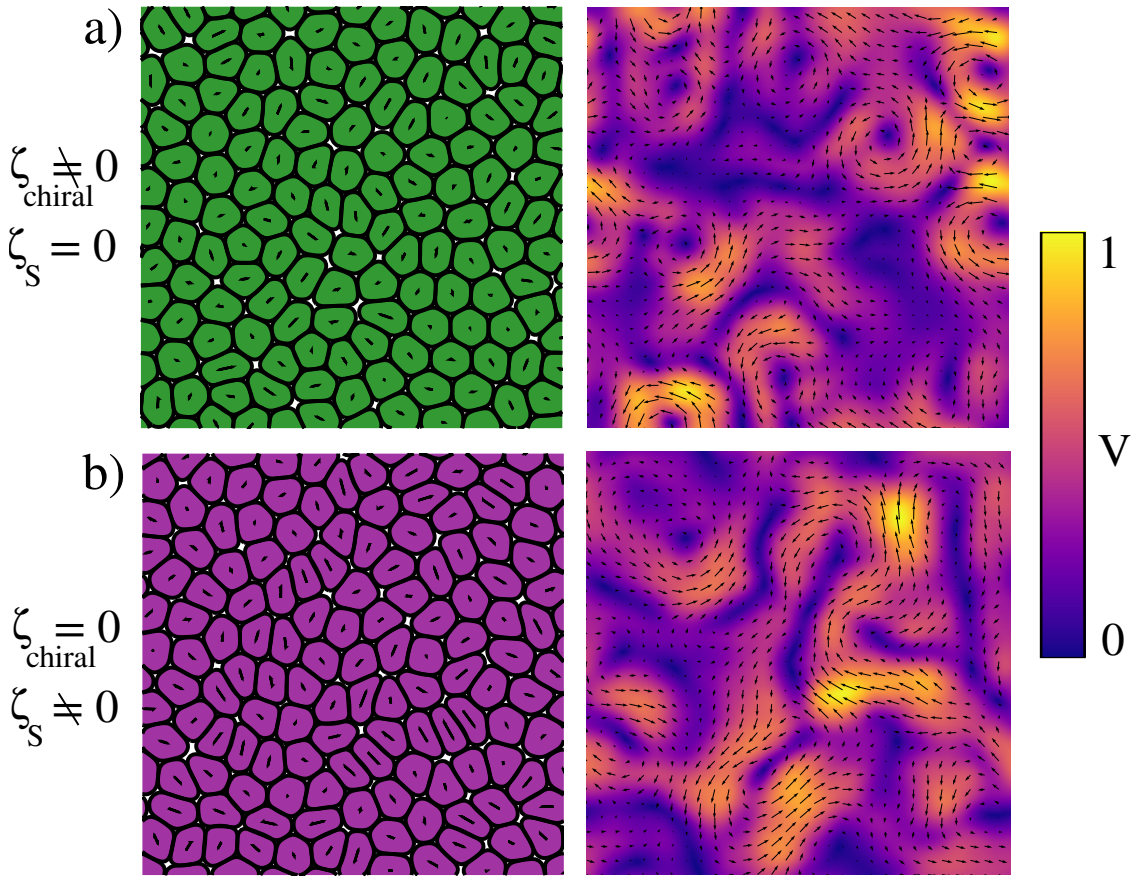

Figure 4.1: Comparison between two simulations performed for achiral and chiral activity respectively both with periodic boundary conditions. a) Left: A plot of the interfaces between cells together with lines indicating the nematic director within them. Right: Velocity distribution v with the colour map representing the magnitude of the velocity field. Magenta being the lowest and yellow being the highest. With the only present activity being chiral $\zeta_{\text{chiral}} = 0.03$, the monolayer tends to organise itself into smaller local vortices as revealed by the velocity field. b) Snapshot from a phase-field simulation of a cellular monolayer with periodic boundary conditions and coefficient of achiral activity $\zeta_S = 0.03$.

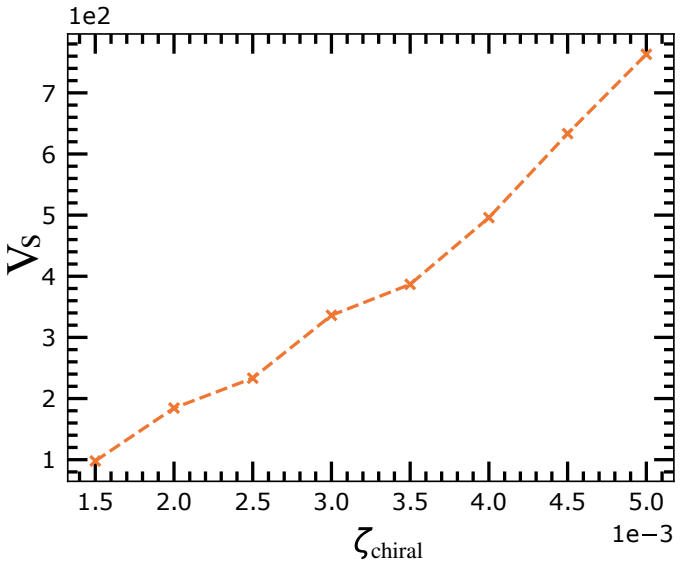

Figure 4.2: Average spaced velocity for large periodic-boundary simulations for simulations with different chiral activities ζ_{chiral}. Increasing chiral activity leads to a more dynamic monolayer.

monolayer remains mostly stationary, and uniformly aligned. At higher ζ_{chiral}, the uniform state, due to the internal stresses, begins to lose stability which results in more active monolayers. This is shown in Fig 4.2, where the averaged-spatial velocity $\mathrm{v_s}$ increases with the chiral activity. The averaged-spactial velocity is given by

$$\mathrm{v_s} = \int_S \sqrt{v_x^2 + v_y^2}\, dS, \tag{4.1}$$

where S is the surface area and $v_{x,y}$ are the velocity components in the x and y direction respectively. Intracellular adhesion has been known to change the dynamics of the monolayer [87], therefore we introduce the adhesion parameter ω from equation 2.2.1, which controls the strength of the intracellular adhesion. Using the same periodic domains and parameters, we add ω in the range $\omega = 0, 0.010, 0.015, 0.020$. Regardless of the adhesion strength, all systems would have an increase in v_{rms} following an increase in chiral activity. Adding cell-cell adhesion to the system also increases the v_{rms} until the threshold $\omega = 0.020$. This can possibly be explained by the adhesion creating small adhesive clusters of cells which act as local vorticies. Increasing ω over a certain threshold hampers the creation of well defined vorticies as cells become too adhesive and are unable to form rotating clusters.

4.2.1 Edge currents

Next, we study monolayers with the same parameters, but in a box with hard walls instead of periodic boundary conditions where the cells are free to slide along the boundary walls

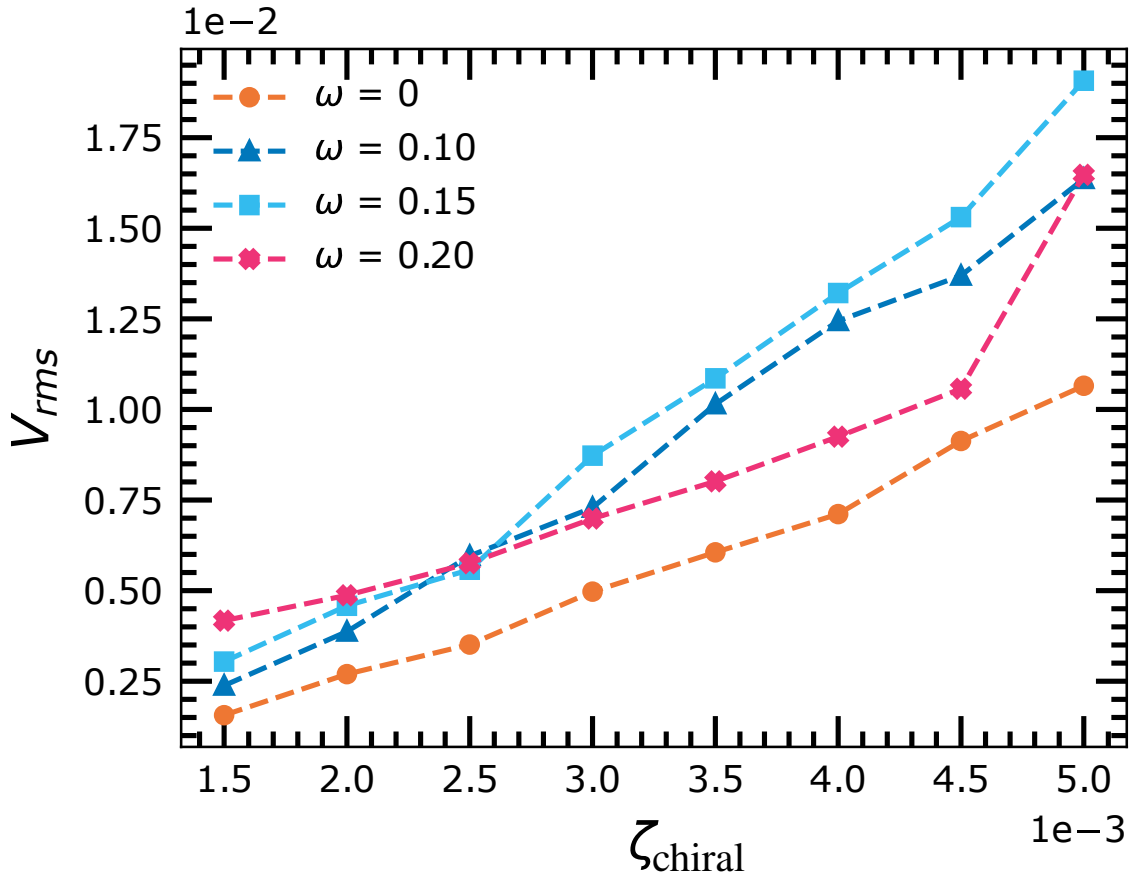

Figure 4.3: Simulations with periodic domains of size 256×265, for different values of chiral activity ζ_{chiral} and cell-cell adhesion ω. Regardless of cell adhesion, higher activity results in higher v_{rms}, and thus, more energy by proxy. Strangely an increase in cell-cell adhesion ω results in an increase in the v_{rms} of the system until the threshold $\omega = 0.20$.

whilst retaining a fixed orientation with respect to them. Introducing the boundary results in radically different dynamics with cells migrating counterclockwise along the boundary, and the collective motion appearing as an edge current (Fig 4.4.a). This is similar to experimental findings presented by Yashunsky et al. in [85]. Although already evident in the velocity field (Fig 4.4.a), we can quantify this by plotting the averaged velocity in the x-direction with respect to the y-direction (Fig 4.4.b). There is a peak at lower values of y and a dip at the highest values of y, effectively showing increased motion, in the form of a current, alongside the edges of the confinement in the counter-clockwise direction.

We extend this study by simulating the monolayer in different geometric confinements. First, we simulate a channel. The channel is defined as having a periodic boundary condition alongside its short boundary, as well as having a hard wall boundary alongside its long boundary. This effectively lets the containing fluid 'flow' through the domain. Fig 4.5.a shows the space and time averaged velocity in the x-direction for the domain in the y-axis. There is a slight increase in velocity alongside the lower and higher values of y giving the impression of a weak edge current alongside the confinement of the domain. Likewise, simulations of the monolayer confined in a long rectangular stripe (Fig 4.5.b), shows clear indications of edge currents similar to the box confinement from Fig 4.4. These additional simulation demonstrate the robustness of these edge currents, as the monolayer is able to organise flow along its confinement in different geometries.

In addition to the box domain, edge currents show up in a variety of different domain geometries including rectangular domains which, similar to the box geometry, have hard walls. Channel domains with hard walls on the long axis and periodic domains on the adjacent shorter axis also display edge current behavior, indicating the edge current is robust in both confined and semi-confined geometries at a range of different parameter values for ζ_{chiral} and channel or rectangular domain width.

4.2.2 Defect flow-field analysis

The argument in [36] states that the presence of chiral active stresses causes a tilt to the flow around $+1/2$ defects. This consequently causes a misalignment between the defect polarity and the direction of motion of the defect, which can lead to its path of motion rotating. Local analysis of the flow-field gives insight into the flow-field behaviour in the vicinity of the $+1/2$ defects. The presence of a symmetric chiral active stress morphs the flow generated by the $+1/2$ defect by deforming and rotating the velocity field surrounding the defect. Fig 4.6 indicates that the flow field which causes the propulsion of the defect, is only on one side of the defect, effectively causing a tilt of the defect. This behaviour is in line with Hoffmann et al.'s statement [36] that the $+1/2$ defects self-propel at a certain angle with respect to their orientation due to the asymmetric flow field around the defect.

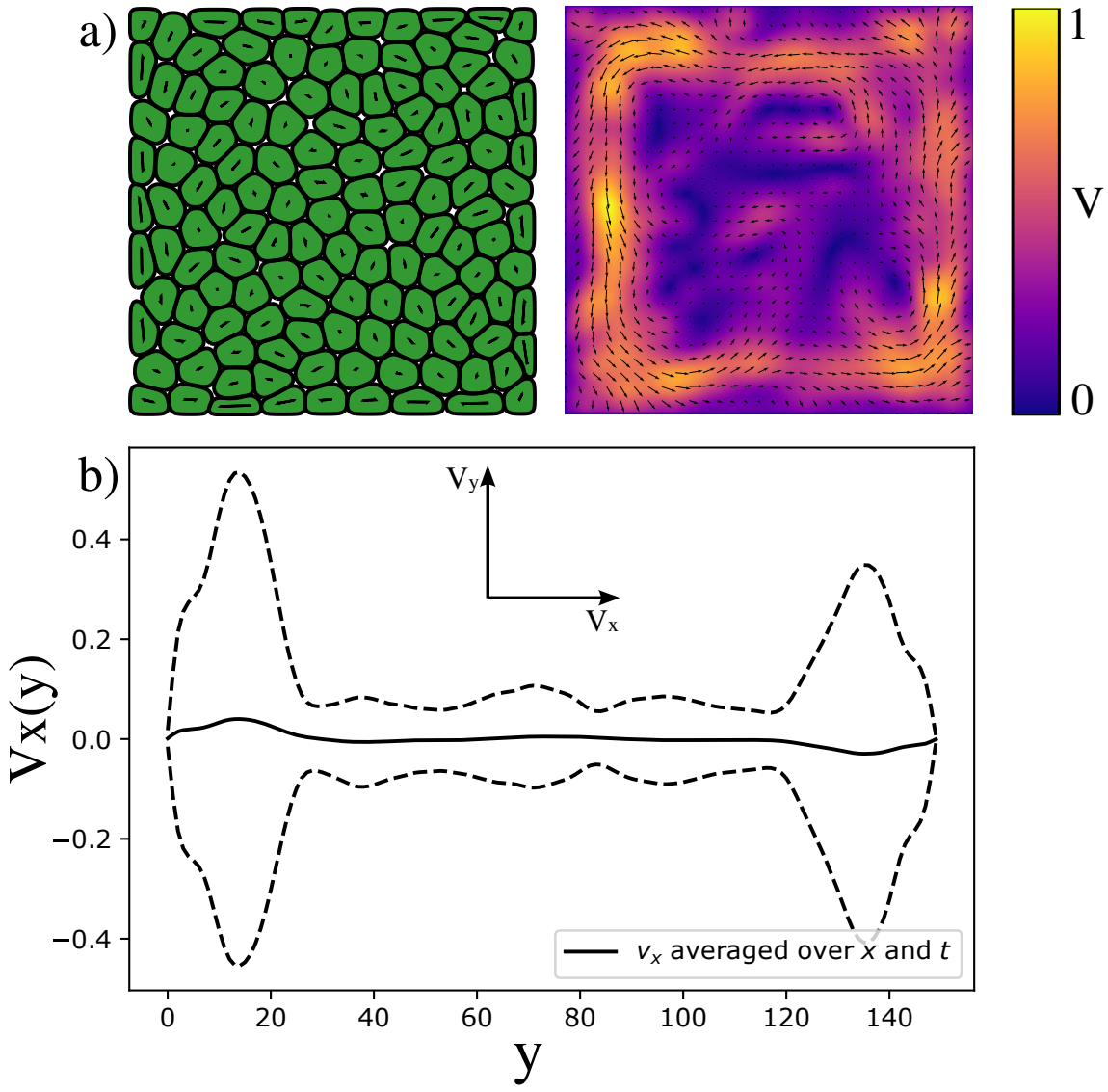

Figure 4.4: a) Snapshot of chiral activity simulation with $\zeta_{\text{chiral}} = 0.03$ in confinement with hard walls (box size: 150×150). Left: visualization of the cell monolayer. Right: Velocity field for the system with the underlying colour-map representing the relative magnitude of velocity. The velocity field indicates a stronger current alongside the edge of the confinement. b) Time and space averaged velocity in the x-direction. The dashed line indicates the corresponding standard deviation. The positive peaks representing v_x at both ends of the x-axis show the presence of an x-directional flow of cells along the top and bottom edge of domain.

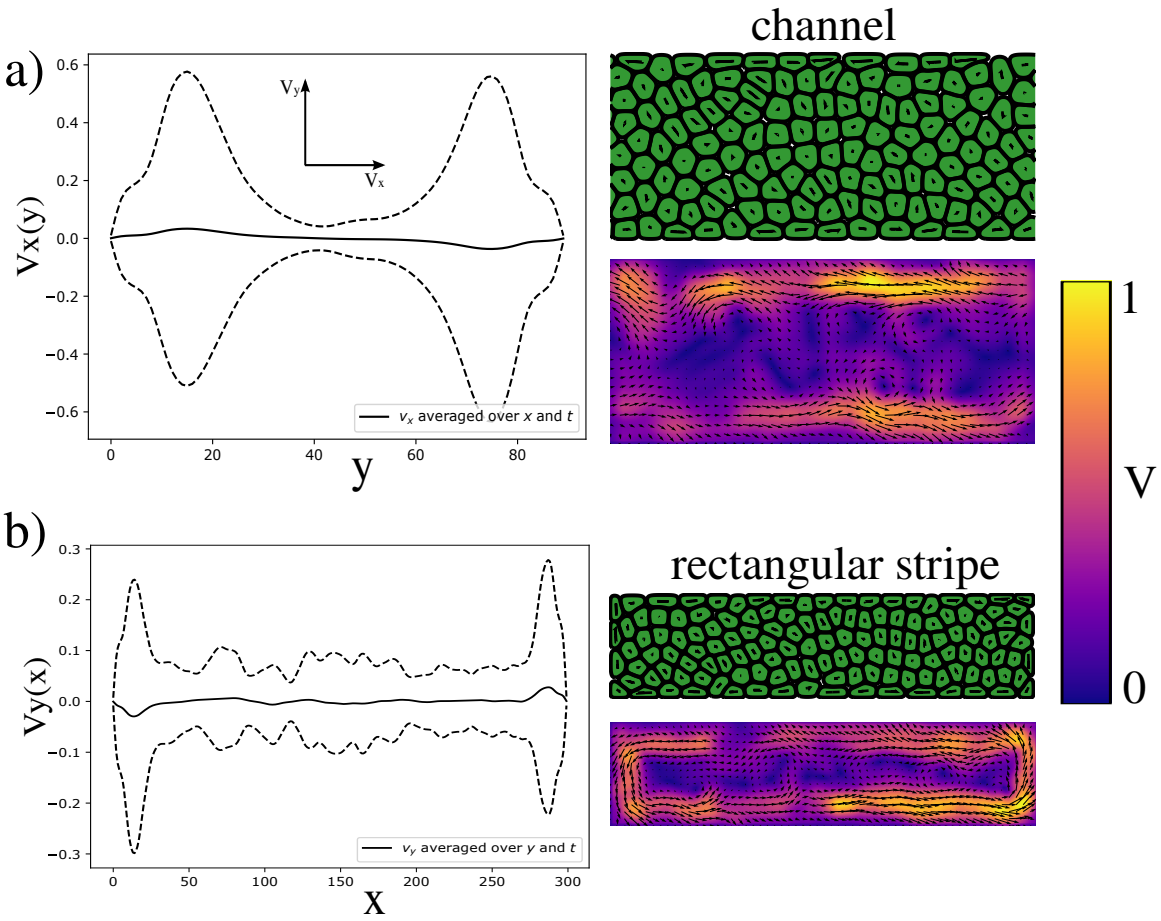

Figure 4.5: Snapshots, velocity field, and corresponding average velocity plots for simulations of a) channel and b) rectangular stripe geometric configurations with $\zeta_{\text{chiral}} = 0.03$. The channel configuration (domain size: 250×90) has periodic boundaries along its short axis and hard walls as the confinements of its long axis. Left: Averaged velocity in the x-direction. Right: Visualization of cell monolayer as well as the velocity field for the system with the underlying colour-map representing the relative magnitude of velocity. The rectangular stripe (domain size: 300×75) is a confined domain with a long axis and a short axis. The averaged velocity is in the y-direction. The dashed line indicates the corresponding standard deviation. The peaks and dips in both average velocity plots indicates the presence of a counter-clockwise flow of cells along the confined edges of the domains.

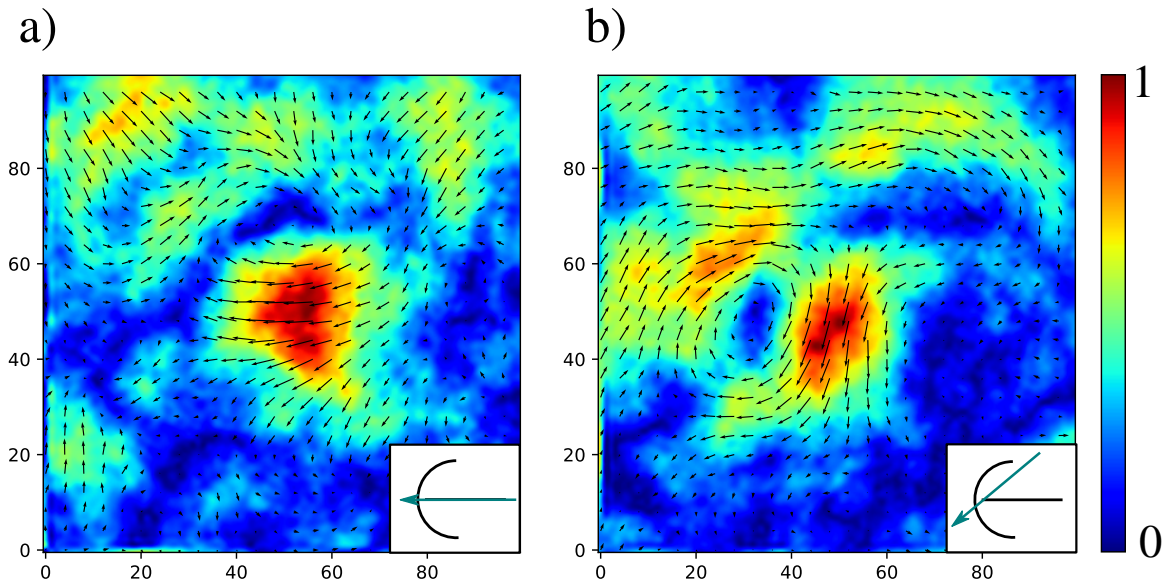

Figure 4.6: Averaged velocity flow field averaged over time for a confined monolayer (box size 150×150) with activity $\zeta_s = 0.03$ for a) achiral stresses only and b) chiral stresses only. The underlying colour map represents the magnitude of the flow field velocity. Plot inserts show the direction of motion for a $+1/2$ defect. Achiral stresses would propel the defect forward as a result of the flow field. The flowfield created by chiral stresses are positioned to tilt the defect from its direction of motion and change its alignment.

4.3 Conclusion

In conclusion, we were able to successfully introduce chiral stresses to a phase-field model of a dense cellular monolayer. Simulations using this model managed to recreate recent experimental results from [85] and demonstrate chiral edge migration of the monolayer alongside the confinement of the domain. These edge current were shown to be robust as they appear under various geometric configurations. Analysis of the flow-field surrounding a defect reveals a tilt in the flow around $+1/2$ topological defects, in agreement with [36]. Furthermore, we find that adding a cell-cell adhesion can, within a certain threshold, lead to more lively dynamics of the monolayer. The findings in this study give numerical context to the analysis in [36] and the experimental assays in [85] and could lead to further questions regarding the coupling of biological organisation of cell systems and active nematics. One exciting evolution of this project could be to look at systems of a monolayer with half of the cells taking one value of chiral activity and the other half a different value of chiral activity. This could give insights into pattern formations during a battle for governance of the collective dynamics in the monolayer.

Chapter 5

Conclusion and outlook

5.1 Summary of conclusions

The thesis explores the collective behavior of active fluid systems after introducing new activity terms in both a continuum and phase-field description of an active system. As a whole, it is found that introducing the new quadrupolar activity ζ_2 and the chiral activity ζ_{chiral} results in a significant impact on the motion of their respective systems. Thus, this thesis contributes to a more complete understanding of activity induced patterns in active systems for the quadrupolar activity ζ_2 and the chiral activity ζ_{chiral}. By implementing these activities into the tool framework, the work in this thesis also contributes to a more complete framework for simulating active fluids. We can draw further conclusion from both of the individual studies that comprise this thesis:

1. In Chapter 3 we use a continuum model to numerically simulate active matter in the presence of hydrodynamic screening, known as dry active nematics. By adding a new quadrupolar active stress, meant to have a stabilizing effect on the system dynamics, we can draw two conclusions. Firstly, we have numerical context to support the linear stability analysis given in [48]. We clearly find that the quadrupolar term indeed has stabilising effects on active systems as increasing the quadrupolar activity term correlates with stabilization of the system. Secondly, the work reveals the emergence of new phases of self-organising behaviour. The phases include polar and nematic ordering of defects, as well as exotic phases of self-organisation, with topological defects forming chains and aster-like structures. These results could further supplement studies into taming active turbulent systems. Additionally, it can support experimental assays in which the stabilizing effects of the quadrupolar force are explored. Finally, the work could lead to experimental endeavors exploring the exotic phases unveiled numerically in this thesis.

2. In Chapter 4 we add a new chiral activity to a phase-field model of cellular monolayer. We find that the chiral activity create vorticies in the monolayer. Flow-field analysis shows that the addition of a chiral stress induces a tilt on the flow surrounding $+1/2$ topological defects.

   When this system is placed in a confinement we find that, similar to other prior experimental results [85] we were able to, by virtue of our model, numerically reproduce the phenomena of collective cell migration within the monolayer as it organises with chiral edge currents along the borders of its confinement. We find that these edge currents are robust and exist in a variety of geometric configurations including channels and rectangular stripes.

5.2 Outlook

Investigating the quadrupolar force in Chapter 3 using a dry continuum model yielded a number of new exotic phases such as systems with defect chain formation and defect asters. It could be interesting to see what states of self-organisation could form when enforcing different geometric boundary conditions on the system. Another possible extension of the project would be to explore the stabilising effects of the quadrupolar force in wet dynamics. Having contributing hydrodynamics effects could lead to completely different collective behaviour.

The topic presented in Chapter 4 is work in progress and the project can evolve in multiple exciting directions. It is promising that we are, using a cell-based approach, able to reproduce similar phenomenology as in experiments and in continuum modeling [85, 36]. This indicates that this framework can be a strong tool for multiscale modeling bridging scale of the cell to the scale of the tissue. One possible extension of this project would be to investigate the behaviour in a system where the cells are two different phases rather than one. Another evolution could look into the effects of a chiral stress on the collective shape of a cluster colony of cells in a free interface. This could give insight into the governing properties of complicated cell monolayers which are made up of cells with different activity strengths.

Simulations using theoretical models are limited in many regards such as computing power and model complexity. It is therefore important to couple theory and experiment in order to archive a complete understanding of the properties of active materials. A greater understanding of the governing properties of active materials can help in the ability to control biological systems which have inherent chaotic behaviour. This could have exciting opportunities in many fields ranging from microscopic drug delivery to a greater understanding of the cell behaviour at the morphogenesis stage of embryo formation.

Bibliography

[1] Supplementary Movies. `https://www.dropbox.com/sh/alwauc0joang94r/AAC2_Ue1Db9W2e1wx406Iwzga?dl=0`.

[2] R. Aditi Simha and Sriram Ramaswamy. Hydrodynamic fluctuations and instabilities in ordered suspensions of self-propelled particles. *Physical Review Letters*, 89:058101, Jul 2002.

[3] R. Aditi Simha and Sriram Ramaswamy. Hydrodynamic fluctuations and instabilities in ordered suspensions of self-propelled particles. *Physical Review Letters*, 89:058101, Jul 2002.

[4] José Alvarado, Bela M. Mulder, and Gijsje H. Koenderink. Alignment of nematic and bundled semiflexible polymers in cell-sized confinement. *Soft Matter*, 10(14):2354–2364, 2014.

[5] Aboutaleb Amiri, Romain Mueller, and Amin Doostmohammadi. Unifying polar and nematic active matter: emergence and co-existence of half-integer and full-integer topological defects. *Journal of Physics A: Mathematical and Theoretical*, 55(9):094002, feb 2022.

[6] Igor S. Aranson, editor. *Physical Models of Cell Motility*. Springer International Publishing, 2016.

[7] Lakshmi Balasubramaniam, Amin Doostmohammadi, Thuan Beng Saw, Gautham Hari Narayana Sankara Narayana, Romain Mueller, Tien Dang, Minnah Thomas, Shafali Gupta, Surabhi Sonam, Alpha S. Yap, Yusuke Toyama, René-Marc Mège, Julia M. Yeomans, and Benoît Ladoux. Investigating the nature of active forces in tissues reveals how contractile cells can form extensile monolayers. *Nature Materials*, 20(8):1156–1166, 2021.

[8] Teagan E. Bate, Edward J. Jarvis, Megan E. Varney, and Kun-Ta Wu. Collective dynamics of microtubule-based 3d active fluids from single microtubules. *Soft Matter*, 15:5006–5016, 2019.

[9] Tobias Bäuerle, Robert C. Löffler, and Clemens Bechinger. Formation of stable and responsive collective states in suspensions of active colloids. *Nature Communications*, 11(1), May 2020.

[10] A. N. Beris and B. J. Edwards. *Thermodynamics of Flowing Systems*. Oxford University Press, 1994.

[11] C Blanch-Mercader, V Yashunsky, S Garcia, G Duclos, L Giomi, and Pascal Silberzan. Turbulent dynamics of epithelial cell cultures. *Physical Review Letters*, 120(20):208101, 2018.

[12] Matthew L. Blow, Sumesh P. Thampi, and Julia M. Yeomans. Biphasic, lyotropic, active nematics. *Physical Review Letters*, 113:248303, Dec 2014.

[13] Agustí Brugués, Ester Anon, Vito Conte, Jim H Veldhuis, Mukund Gupta, Julien Colombelli, JoséJ Muñoz, G Wayne Brodland, Benoit Ladoux, and Xavier Trepat. Forces driving epithelial wound healing. *Nat Phys*, 10(9):683–690, Sep 2014.

[14] Hugues Chaté. Dry aligning dilute active matter. *Annual Review of Condensed Matter Physics*, 11(1):189–212, 2020.

[15] Peter J Collings and John W Goodby. *Introduction to liquid crystals*. CRC Press, London, England, 2 edition, October 2019.

[16] Jordi Comelles, Soumya SS, Linjie Lu, Emilie Le Maout, S Anvitha, Guillaume Salbreux, Frank Jülicher, Mandar M Inamdar, and Daniel Riveline. Epithelial colonies in vitro elongate through collective effects. *eLife*, 10, January 2021.

[17] Adama Creppy, Olivier Praud, Xavier Druart, Philippa L. Kohnke, and Franck Plouraboué. Turbulence of swarming sperm. *Phys. Rev. E*, 92:032722, Sep 2015.

[18] Pierre-Gilles De Gennes and Jacques Prost. *The physics of liquid crystals*, volume 83. Oxford university press, 1993.

[19] Amin Doostmohammadi, Michael F Adamer, Sumesh P Thampi, and Julia M Yeomans. Stabilization of active matter by flow-vortex lattices and defect ordering. *Nat. Comm.*, 7:10557, 2016.

[20] Amin Doostmohammadi, Jordi Ignés-Mullol, Julia M Yeomans, and Francesc Sagués. Active nematics. *Nature communications*, 9(1):1–13, 2018.

[21] Amin Doostmohammadi and Benoit Ladoux. Physics of liquid crystals in cell biology. *Trends in Cell Biology*, 32(2):140–150, 2022.

[22] Amin Doostmohammadi and Julia M. Yeomans. Coherent motion of dense active matter. *The European Physical Journal Special Topics*, 227(17):2401–2411, March 2019.

[23] G Duclos, C Blanch-Mercader, V Yashunsky, G Salbreux, J-F Joanny, J Prost, and Pascal Silberzan. Spontaneous shear flow in confined cellular nematics. *Nature physics*, 14(7):728–732, 2018.

[24] Guillaume Duclos, Christoph Erlenkämper, Jean-François Joanny, and Pascal Silberzan. Topological defects in confined populations of spindle-shaped cells. *Nature Physics*, 13(1):58–62, 2017.

[25] Guillaume Duclos, Christoph Erlenkämper, Jean-François Joanny, and Pascal Silberzan. Topological defects in confined populations of spindle-shaped cells. *Nature Physics*, 13(1):58–62, January 2017.

[26] Brian J. Edwards, Antony N. Beris, and Miroslav Grmela. Generalized constitutive equation for polymeric liquid crystals part 1. model formulation using the hamiltonian (poisson bracket) formulation. *Journal of Non-Newtonian Fluid Mechanics*, 35(1):51–72, 1990.

[27] Peter Friedl, Joseph Locker, Erik Sahai, and Jeffrey E Segall. Classifying collective cancer cell invasion. *Nat Cell Biol*, 14(8):777–783, Aug 2012.

[28] Simon Garcia, Edouard Hannezo, Jens Elgeti, Jean-François Joanny, Pascal Silberzan, and Nir S. Gov. Physics of active jamming during collective cellular motion in a monolayer. *Proceedings of the National Academy of Sciences*, 112(50):15314–15319, 2015.

[29] Luca Giomi, Mark J Bowick, Xu Ma, and M Cristina Marchetti. Defect annihilation and proliferation in active nematics. *Physical Review Letters*, 110(22):228101, 2013.

[30] Maria Grazia Giordano, Francesco Bonelli, Livio Nicola Carenza, Giuseppe Gonnella, and Giuseppe Negro. Activity-induced isotropic-polar transition in active liquid crystals. *EPL (Europhysics Letters)*, 133(5):58004, 2021.

[31] Gerhard Gompper, Roland G Winkler, Thomas Speck, Alexandre Solon, Cesare Nardini, Fernando Peruani, Hartmut Löwen, Ramin Golestanian, U Benjamin Kaupp, Luis Alvarez, Thomas Kiørboe, Eric Lauga, Wilson C K Poon, Antonio DeSimone, Santiago Muiños-Landin, Alexander Fischer, Nicola A Söker, Frank Cichos, Raymond Kapral, Pierre Gaspard, Marisol Ripoll, Francesc Sagues, Amin Doostmohammadi, Julia M Yeomans, Igor S Aranson, Clemens Bechinger, Holger Stark, Charlotte K Hemelrijk, François J Nedelec, Trinish Sarkar, Thibault Aryaksama, Mathilde Lacroix, Guillaume Duclos, Victor Yashunsky, Pascal Silberzan, Marino Arroyo, and Sohan Kale. The 2020 motile active matter roadmap. *Journal of Physics: Condensed Matter*, 32(19):193001, feb 2020.

[32] Robert Großmann, Fernando Peruani, and Markus Bär. Mesoscale pattern formation of self-propelled rods with velocity reversal. *Physical Review E*, 94:050602, Nov 2016.

[33] Pau Guillamat, Jordi Ignés-Mullol, and Francesc Sagués. Taming active turbulence with patterned soft interfaces. *Nature communications*, 8(1):1–8, 2017.

[34] Jérôme Hardoüin, Rian Hughes, Amin Doostmohammadi, Justine Laurent, Teresa Lopez-Leon, Julia M Yeomans, Jordi Ignés-Mullol, and Francesc Sagués. Reconfigurable flows and defect landscape of confined active nematics. *Communications Physics*, 2(1):1–9, 2019.

[35] Carl-Philipp Heisenberg and Yohanns Bellaïche. Forces in tissue morphogenesis and patterning. *Cell*, 153(5):948–962, May 2013.

[36] Ludwig A. Hoffmann, Koen Schakenraad, Roeland M. H. Merks, and Luca Giomi. Chiral stresses in nematic cell monolayers. *Soft Matter*, 16(3):764–774, 2020.

[37] Harish P. Jain, Dennis Wenzel, and Axel Voigt. The impact of contact inhibition on collective cell migration and proliferation, 2021.

[38] Frank Jülicher, Stephan W Grill, and Guillaume Salbreux. Hydrodynamic theory of active matter. *Reports on Progress in Physics*, 81(7):076601, 2018.

[39] G Junot, G Briand, R Ledesma-Alonso, and Olivier Dauchot. Active versus passive hard disks against a membrane: mechanical pressure and instability. *Physical Review Letters*, 119(2):028002, 2017.

[40] Kyogo Kawaguchi, Ryoichiro Kageyama, and Masaki Sano. Topological defects control collective dynamics in neural progenitor cell cultures. *Nature*, 545(7654):327–331, 2017.

[41] Felix C Keber, Etienne Loiseau, Tim Sanchez, Stephen J DeCamp, Luca Giomi, Mark J Bowick, M Cristina Marchetti, Zvonimir Dogic, and Andreas R Bausch. Topology and dynamics of active nematic vesicles. *Science*, 345(6201):1135–1139, 2014.

[42] Donald L. Koch and Ganesh Subramanian. Collective hydrodynamics of swimming microorganisms: Living fluids. *Annual Review of Fluid Mechanics*, 43(1):637–659, 2011.

[43] Karsten Kruse, Jean-François Joanny, Frank Jülicher, Jacques Prost, and Ken Sekimoto. Asters, vortices, and rotating spirals in active gels of polar filaments. *Physical Review Letters*, 92(7):078101, 2004.

[44] Nitin Kumar, Harsh Soni, Sriram Ramaswamy, and AK Sood. Flocking at a distance in active granular matter. *Nature Communications*, 5(1):4688, 2014.

[45] Nitin Kumar, Rui Zhang, Juan J de Pablo, and Margaret L Gardel. Tunable structure and dynamics of active liquid crystals. *Science Advances*, 4(10), 2018.

[46] Zhong-Yi Li, De-Qing Zhang, and Bo Li. Formation and propagation of solitonlike defect clusters in confined active nematics with chiral anchoring. *Physical Review Research*, 3:023253, Jun 2021.

[47] Jakob Löber, Falko Ziebert, and Igor S. Aranson. Collisions of deformable cells lead to collective migration. *Scientific Reports*, 5(1), March 2015.

[48] Ananyo Maitra, Pragya Srivastava, M Cristina Marchetti, Juho S Lintuvuori, Sriram Ramaswamy, and Martin Lenz. A nonequilibrium force can stabilize 2d active nematics. *Proceedings of the National Academy of Sciences*, 115(27):6934–6939, 2018.

[49] M. C. Marchetti, J. F. Joanny, S. Ramaswamy, T. B. Liverpool, J. Prost, Madan Rao, and R. Aditi Simha. Hydrodynamics of soft active matter. *Reviews of Modern Physics*, 85:1143–1189, 2013.

[50] Tomer Markovich, Elsen Tjhung, and Michael E Cates. Chiral active matter: microscopic 'torque dipoles' have more than one hydrodynamic description. *New Journal of Physics*, 21(11):112001, nov 2019.

[51] Yonit Maroudas-Sacks, Liora Garion, Lital Shani-Zerbib, Anton Livshits, Erez Braun, and Kinneret Keren. Topological defects in the nematic order of actin fibres as organization centres of hydra morphogenesis. *Nature Physics*, 17(2):251–259, 2021.

[52] A. J. T. M. Mathijssen, A. Doostmohammadi, J. M. Yeomans, and T. N. Shendruk. Hydrodynamics of micro-swimmers in films. *Journal of Fluid Mechanics*, 806:35–70, 2016.

[53] O. J. Meacock, A. Doostmohammadi, K. R. Foster, J. M. Yeomans, and W. M. Durham. Bacteria solve the problem of crowding by moving slowly. *Nature Physics*, 17(2):205–210, November 2020.

[54] Luuk Metselaar, Julia M Yeomans, and Amin Doostmohammadi. Topology and morphology of self-deforming active shells. *Physical Review Letters*, 123(20):208001, 2019.

[55] Romain Mueller, Julia M. Yeomans, and Amin Doostmohammadi. Emergence of active nematic behavior in monolayers of isotropic cells. *Physical Review Letters*, 122:048004, Feb 2019.

[56] Ken H. Nagai. Collective motion of rod-shaped self-propelled particles through collision. *Biophysics and Physicobiology*, 15(0):51–57, 2018.

[57] Daniel Needleman and Zvonimir Dogic. Active matter at the interface between materials science and cell biology. *Nature Reviews Materials*, 2(9):1–14, 2017.

[58] Mehrana Raeisian Nejad, Amin Doostmohammadi, and Julia Mary Yeomans. Memory effects, arches and polar defect ordering at the cross-over from wet to dry active nematics. *Soft Matter*, 17:2500–2511, 2021.

[59] Anand U Oza and Jörn Dunkel. Antipolar ordering of topological defects in active liquid crystals. *New Journal of Physics*, 18(9):093006, 2016.

[60] Jin-Ah Park, Jae Hun Kim, Dapeng Bi, Jennifer A. Mitchel, Nader Taheri Qazvini, Kelan Tantisira, Chan Young Park, Maureen McGill, Sae-Hoon Kim, Bomi Gweon, Jacob Notbohm, Robert Steward Jr, Stephanie Burger, Scott H. Randell, Alvin T. Kho, Dhananjay T. Tambe, Corey Hardin, Stephanie A. Shore, Elliot Israel, David A. Weitz, Daniel J. Tschumperlin, Elizabeth P. Henske, Scott T. Weiss, M. Lisa Manning, James P. Butler, Jeffrey M. Drazen, and Jeffrey J. Fredberg. Unjamming and cell shape in the asthmatic airway epithelium. *Nature Materials*, 14(10):1040–1048, August 2015.

[61] D. J. G. Pearce, J. Nambisan, P. W. Ellis, A. Fernandez-Nieves, and L. Giomi. Orientational correlations in active and passive nematic defects. *Phys. Rev. Lett.*, 127:197801, Nov 2021.

[62] Fernando Peruani, Jörn Starruß, Vladimir Jakovljevic, Lotte Søgaard-Andersen, Andreas Deutsch, and Markus Bär. Collective motion and nonequilibrium cluster formation in colonies of gliding bacteria. *Phys. Rev. Lett.*, 108:098102, Feb 2012.

[63] Fernando Peruani, Jörn Starruß, Vladimir Jakovljevic, Lotte Søgaard-Andersen, Andreas Deutsch, and Markus Bär. Collective motion and nonequilibrium cluster formation in colonies of gliding bacteria. *Physical Review Letters*, 108:098102, Feb 2012.

[64] M. Poujade, E. Grasland-Mongrain, A. Hertzog, J. Jouanneau, P. Chavrier, B. Ladoux, A. Buguin, and P. Silberzan. Collective migration of an epithelial monolayer in response to a model wound. *Proceedings of the National Academy of Sciences*, 104(41):15988–15993, 2007.

[65] Elias Putzig, Gabriel S Redner, Arvind Baskaran, and Aparna Baskaran. Instabilities, defects, and defect ordering in an overdamped active nematic. *Soft matter*, 12(17):3854–3859, 2016.

[66] Tim Sanchez, Daniel TN Chen, Stephen J DeCamp, Michael Heymann, and Zvonimir Dogic. Spontaneous motion in hierarchically assembled active matter. *Nature*, 491(7424):431–434, 2012.

[67] T. B. Saw, A. Doostmohammadi, V. Nier, L. Kocgozlu, S. Thampi, Y. Toyama, P. Marcq, C. T Lim, J. M. Yeomans, and B. Ladoux. Topological defects in epithelia govern cell death and extrusion. *Nature*, 544:212–216, 2017.

[68] Christian Scholz, Michael Engel, and Thorsten Pöschel. Rotating robots move collectively and self-organize. *Nature Communications*, 9(1):1497, 2018.

[69] Suraj Shankar and M Cristina Marchetti. Hydrodynamics of active defects: from order to chaos to defect ordering. *Physical Review X*, 9(4):041047, 2019.

[70] Suraj Shankar, Sriram Ramaswamy, M Cristina Marchetti, and Mark J Bowick. Defect unbinding in active nematics. *Physical Review Letters*, 121(10):108002, 2018.

[71] Suraj Shankar, Anton Souslov, Mark J. Bowick, M. Cristina Marchetti, and Vincenzo Vitelli. Topological active matter, 2021.

[72] Salik A. Sultan, Mehrana R. Nejad, and Amin Doostmohammadi. Quadrupolar active stress induces exotic phases of defect motion in active nematics. 2021.

[73] Dennis J. Ternet, Ronald G. Larson, and L. Gary Leal. Flow-aligning and tumbling in small-molecule liquid crystals: pure components and mixtures. *Rheologica Acta*, 38(3):183–197, 1999.

[74] S. P. Thampi and J. M. Yeomans. Active turbulence in active nematics. *The European Physical Journal Special Topics*, 225(4):651–662, 2016.

[75] Sumesh P Thampi, Amin Doostmohammadi, Ramin Golestanian, and Julia M Yeomans. Intrinsic free energy in active nematics. *EPL (Europhysics Letters)*, 112(2):28004, 2015.

[76] Sumesh P Thampi, Ramin Golestanian, and Julia M Yeomans. Instabilities and topological defects in active nematics. *EPL (Europhysics Letters)*, 105(1):18001, 2014.

[77] Kristian Thijssen, Mehrana R. Nejad, and Julia M. Yeomans. Role of friction in multidefect ordering. *Physical Review Letters*, 125:218004, Nov 2020.

[78] John Toner and Yuhai Tu. Flocks, herds, and schools: A quantitative theory of flocking. *Physical Review E*, 58:4828–4858, Oct 1998.

[79] Taras Turiv, Runa Koizumi, Kristian Thijssen, Mikhail M. Genkin, Hao Yu, Chenhui Peng, Qi-Huo Wei, Julia M. Yeomans, Igor S. Aranson, Amin Doostmohammadi, and Oleg D. Lavrentovich. Polar jets of swimming bacteria condensed by a patterned liquid crystal. *Nature Physics*, 16(4):481–487, March 2020.

[80] Farzan Vafa, Mark J. Bowick, Boris I. Shraiman, and M. Cristina Marchetti. Fluctuations can induce local nematic order and extensile stress in monolayers of motile cells. *Soft Matter*, 17(11):3068–3073, 2021.

[81] R Voituriez, Jean-François Joanny, and Jacques Prost. Spontaneous flow transition in active polar gels. *EPL (Europhysics Letters)*, 70(3):404, 2005.

[82] Kimberly L Weirich, Kinjal Dasbiswas, Thomas A Witten, Suriyanarayanan Vaikuntanathan, and Margaret L Gardel. Self-organizing motors divide active liquid droplets. *Proceedings of the National Academy of Sciences*, 116(23):11125–11130, 2019.

[83] Hugo Wioland, Enkeleida Lushi, and Raymond E Goldstein. Directed collective motion of bacteria under channel confinement. *New Journal of Physics*, 18(7):075002, 2016.

[84] Kun-Ta Wu, Jean Bernard Hishamunda, Daniel T. N. Chen, Stephen J. DeCamp, Ya-Wen Chang, Alberto Fernández-Nieves, Seth Fraden, and Zvonimir Dogic. Transition from turbulent to coherent flows in confined three-dimensional active fluids. *Science*, 355(6331), March 2017.

[85] V. Yashunsky, D. J. G. Pearce, C. Blanch-Mercader, F. Ascione, L. Giomi, and P. Silberzan. Chiral edge currents in confined fibrosarcoma cells. 2020.

[86] Guanming Zhang, Romain Mueller, Amin Doostmohammadi, and Julia M. Yeomans. Active inter-cellular forces in collective cell motility. *Journal of The Royal Society Interface*, 17(169):20200312, August 2020.

[87] Falko Ziebert and Igor S. Aranson. Effects of adhesion dynamics and substrate compliance on the shape and motility of crawling cells. *PLOS ONE*, 8(5):1–14, 05 2013.